

Article

Origin and Paleoenvironmental Conditions of the Köprübaşı Evaporites (Eastern Anatolia, Turkey): Sedimentological, Mineralogical and Geochemical Constraints

Pelin Güngör Yeşilova ^{1,*} and Ozan Baran ²¹ Department of Geological Engineering, Engineering Faculty, Van Yüzüncü Yıl University, 65080 Van, Turkey² Institute of Natural Applied Sciences, Van Yüzüncü Yıl University, 65080 Van, Turkey

* Correspondence: pelingungoryesilova@yyu.edu.tr

Abstract: Köprübaşı evaporites mainly consist of primary (selenite and gypsarenite) and secondary (massive, laminated and satin-spar) gypsum lithofacies, as well as minor anhydrite, and are interbedded with clastic and carbonate units. Sedimentological-mineralogical and geochemical findings reveal that the depositional basin extends from a lagoon to the hinterland. These data confirm that too much detrital input was transported into the basin with multiple salinity and pH value fluctuations, organic matter activity and reducing conditions. Geochemical data point out the shallow environment and the mixing of hydrothermal fluids and fresh waters. The investigated evaporites were exposed to diagenesis and alteration under the influence of a hot—dry and minor humid climate, tectonism and pressure. The ⁸⁷Sr/⁸⁶Sr, δ³⁴S and δ¹⁸O isotope values of Köprübaşı evaporites reveal that they are of Miocene marine sulfate origin.

Keywords: Eastern Anatolia; Başkale; Van; Köprübaşı evaporite; marine origin



Citation: Güngör Yeşilova, P.; Baran, O. Origin and Paleoenvironmental Conditions of the Köprübaşı Evaporites (Eastern Anatolia, Turkey): Sedimentological, Mineralogical and Geochemical Constraints. *Minerals* **2023**, *13*, 282. <https://doi.org/10.3390/min13020282>

Academic Editors: Roberto Buccione and Rabah Kechiched

Received: 21 January 2023

Revised: 13 February 2023

Accepted: 15 February 2023

Published: 17 February 2023



Copyright: © 2023 by the authors. Licensee MDPI, Basel, Switzerland. This article is an open access article distributed under the terms and conditions of the Creative Commons Attribution (CC BY) license (<https://creativecommons.org/licenses/by/4.0/>).

1. Introduction

Evaporites are one of the most important rock groups used to explain the paleoenvironmental conditions of the basins. Evaporites give important clues about the temperature, climate and water chemistry of ancient marine (such as lagoons and coastal sabkha) and terrestrial (salt lakes, salt pan and continental sabkha) environments [1,2].

The Eastern Anatolia region has a complicated tectonic structure that developed as a result of the collision of the Eurasian and Arabian plates (Figure 1a) [3,4]. Therefore, the region contains E–W trending and pull-apart basins originating from N–S trending compression [5]. In the Van–Başkale Basin, which is one of these basins formed by the effect of compression, the older units were folded and superimposed on each other, and then faulted by strike-slip faults and thrusts (Figure 1b) [6,7].

Many stratigraphic, mapping, oil exploration and tectonic studies have been carried out in the Başkale Basin and its surroundings, e.g., [6,8–13]. However, there has been no previous study on the Köprübaşı evaporites, which are located in the southwest of this basin and constitute the main subject of this study (Figure 1b,c). Therefore, this study is important as it will contribute to the correlation and identification of formations of similar origin both in the Eastern Anatolia region and globally.

The aim of this study is to determine the origin of the evaporites of the Başkale Basin and reveal the paleoenvironmental conditions by sedimentological, petrographical—mineralogical and geochemical data.

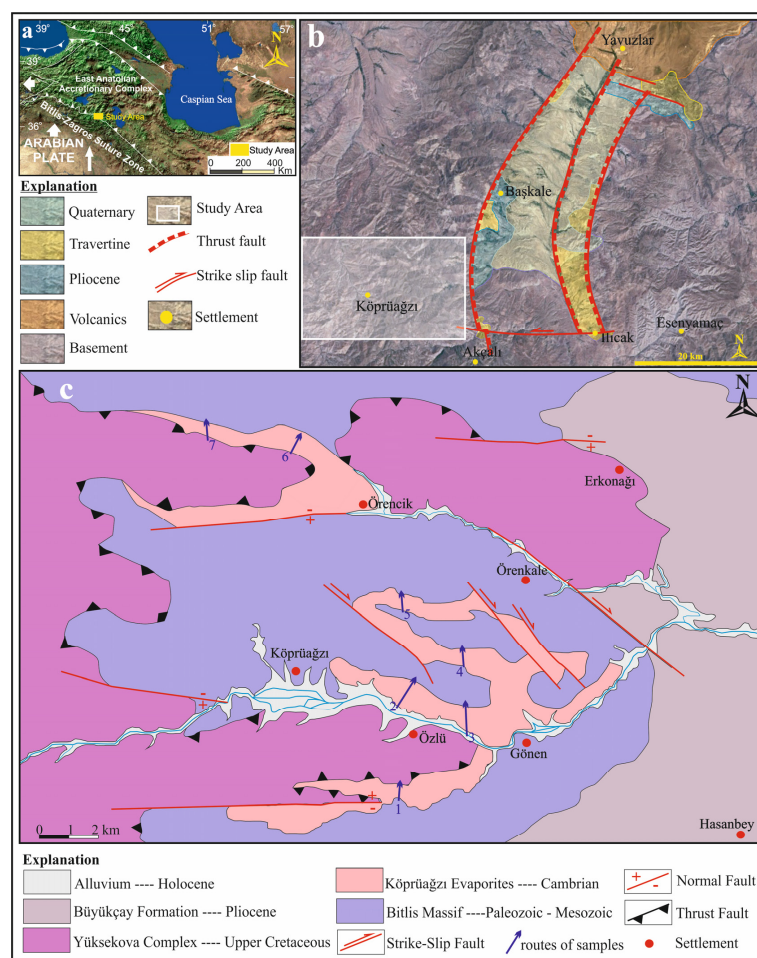


Figure 1. (a) Location of the study area in Eastern Anatolia, (b) location of the study area in the Başkale Basin (modified from [13]). (c) Geological map and stratigraphy of the study area.

2. Geological Settings

The Eastern Anatolia region is formed by the closure of the southern branch of Neotethys along the Bitlis–Zagros Suture Zone (BZSZ) after the collision of the Arabian and Eurasian plates before or during the Early Miocene [14,15] (Figure 1a). The region contains extensive accretionary units and large crystalline massifs [16]. The Eastern Anatolian plateau is located at the intersection of several continental blocks: the Eastern Pontides in the north, the Bitlis Massif and the Arabian Platform in the south, the Menderes-Taurus block in the west and the northwest Iranian block in the east [17]. The Bitlis Massif is the equivalent of the Central Iranian Massif metamorphics continuing eastward towards Iran’s Sanandaj–Sirjan region, forming the southern continental margin of the Anatolian–Iranian platform [18,19]. The Başkale Basin is located in the southeast of the Lake Van Basin in Eastern Anatolia in the eastern section of the southeast Taurus orogenic belt and on the Turkish–Iranian border (Figure 1a,b). Köprüağzı evaporites in the study area outcrop in Gönen, Köprüağzı, Örenkale and Erkonagı villages and surroundings located nearly 15 km southwest in the Başkale Basin (Figure 1c). The study area contains the southwest of the Başkale Basin, which comprises allochthonous and autochthonous units [9]. These units were thrust on each other from north to south after or during the Miocene due to intense tectonic movements [9,10] (Figure 2a). The Başkale Basin was a marine environment in the Paleozoic, while the continental environment developed in the Triassic, Jurassic and Early Cretaceous [20]. After this regression, the environment became marine in the Late Cretaceous. The basement of the study area comprises an allochthonous unit of the Paleozoic (Precambrian–Early Paleozoic) Bitlis Massif [12,21,22] (Figures 1c and 2a). References [23,24] suggest that these rocks were deposited, deformed and metamorphosed

in the Paleozoic (Figure 2a). In most parts of the study area, these metamorphic rocks were folded (Figure 2c). These units consist of phyllites, schist, amphibolite, metaquartzite and recrystallized limestone to the southwest of the Köprüağzı village (Figure 2a,c,d). The Köprüağzı evaporites were observed as mixed with Bitlis Massif metamorphics, and the lower levels of these evaporites contained metamorphic blocks (Figures 1c and 2a,c,d). Lithologies of both the Bitlis Massif and Köprüağzı evaporites were affected by regional tectonism. These evaporites were generally observed as intercalating with carbonate—rich (black dolomitic limestones and yellow limestone) and clastic material—rich (claystone, sandstone, red mudstone and conglomerate) units. These evaporites were overlain by Yüksekova Ophiolitic Complex (Figures 1c and 2a,b,e). The upper parts of these evaporites contained blocks belonging to the Yüksekova complex (Figure 2a,b). These ophiolitic units outcrop in a broad area between the Köprüağzı, Örenkale and Gönen villages and mainly contain serpentinite, radiolarite and peridotite rocks (Figures 1c and 2b,e). Along with this, these allochthonous units were covered by Neogene autochthonous units in the field (Figure 1c). These units include claystones, siltstones and conglomerates of the Pliocene Büyükçay Formation. The youngest unit in the study area was the recent Holocene formed by the Köprüağzı Stream, which unconformably overlies all these units (Figure 1c).

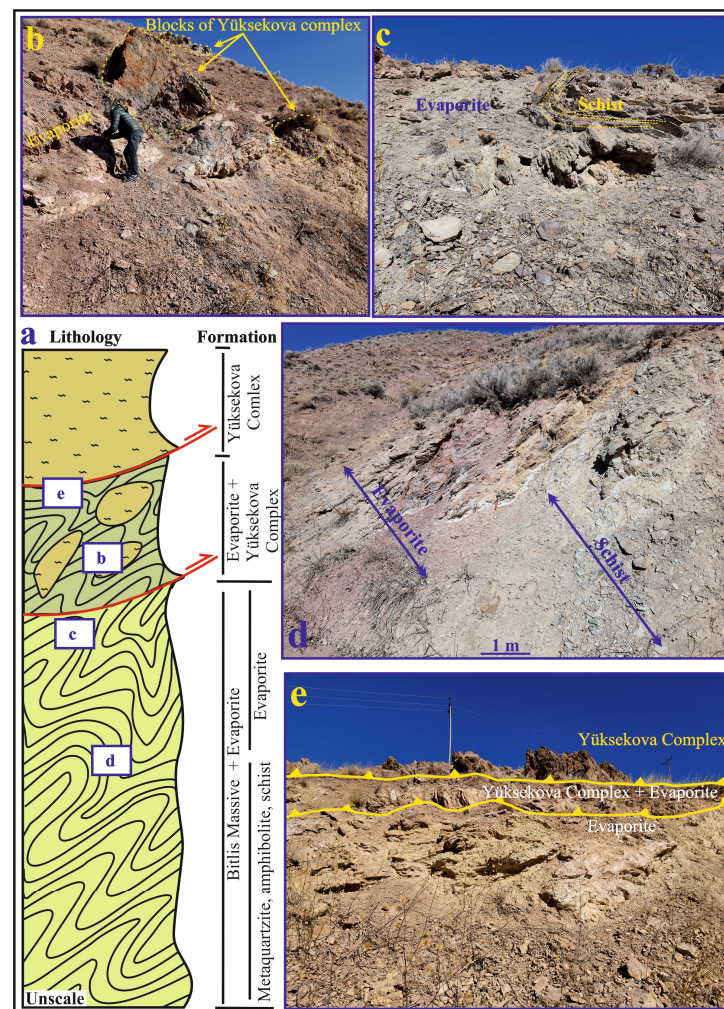


Figure 2. (a) The cross section showing stratigraphic relationships of the units in the study area; (b) Evaporitic units containing blocks belonging to the Yüksekova Complex; (c) Evaporitic units containing folded schist blocks belonging to the Bitlis massif; (d) Evaporites mixed with Bitlis Massif metamorphics; (e) Yüksekova Complex, tectonically overlying the evaporates (The letters shown in the box in the section indicate the figures corresponding to the same letter on the cross section).

3. Methodology

During the fieldwork, a total of 60 clay, mud, sand and carbonate intercalating with primary and secondary gypsum samples were collected around the Köprüağzı (K), Örenkale (O), Örencik (B) and Gönen (OBK) villages.

Non-fractured and unaltered samples were chosen for geochemical analyses. Petrographical–mineralogical studies were performed by using a polarizing microscope (Dokuz Eylül University Thin Section Laboratory, İzmir, Turkey) and a scanning electron microscope (SEM-EDS) (Scientific Research and Application Center, Van Yüzüncü Yıl University, Van, Turkey). The prepared natural surface fracture type and polished section samples were covered with Au-Pd for 90 s, examined with a ZEISS Sigma 300 model SEM microscope and photographed with an SE2 detector. X-ray Diffraction (XRD) whole-rock analysis was conducted in the Earth Sciences Research and Application Center of Ankara University (Ankara, Turkey). The results of these analyses are shown in graphs.

The element analysis (major and trace elements) of 10 evaporite samples was made in the Earth Science Research Center of Ankara University (Ankara, Turkey). These samples were measured in X-ray Fluorescence (XRF) spectroscopy. This spectrometer performs quantitative analysis of elements with atomic numbers between 9 and 92. It cannot study elements with atomic numbers less than 9 and is not sensitive enough in the degree of chemical bonding. The XRF generally operates at 50 kV and 50 mA. Using an X-ray Fluorescence Spectrometer, the major element oxides such as Si, Al, Ti, Mn and Mg in percent by weight (%), trace elements such as Rb, Ba and Sr and transition elements such as Zr, Ni, Co, Cu and Zn were analyzed at the ppm level (Table 1). The powdered samples were compressed into disks with a variety of binding materials in a hydraulic press and prepared for analysis. Loss on ignition (LOI) was calculated as recommended by [25] and element concentrations were calculated according to STD DS11, STD GS 311–1, STD OREAS262 and STD SO 19 standards.

Table 1. Major (%) and trace element (ppm) values of the different evaporite rock samples intercalated with clastic and carbonate.

Lithology	Anhydrite-Bearing Laminated Gypsum	Massive Gypsum	Satin-Spar	Gypsarenite	Selenite	Massive	Gypsarenite-Bearing Claystone	Laminated Gypsum-Bearing Claystone	Selenite-Bearing Mudstone	Satin-Spar Gypsum-Bearing Carbonate
Sample No	B-11	B-7	K-12	K-8	K-5	O-6	OBK-3	OBK-7	OBK-6	OBK-4
MgO	0.7	3.6	1.1	7.4	1.6	7.5	1.4	2.2	4.5	0.6
Al ₂ O ₃	0.7	1.9	0.08	0.008	0.09	2.9	8.3	3.3	3.4	4.9
SiO ₂	3.5	9.8	3.8	6.5	2.2	20	11.5	11	13.9	10.3
P ₂ O ₅	0.003	0.09	0.11	0.02	0.08	0.05	0.38	0.08	0.18	0.14
SO ₃	0.1	23.4	38.2	15.6	38.5	2.7	33.8	30.1	24.2	36.3
K ₂ O	0.4	0.5	0.007	0.005	0.006	0.9	0.3	0.1	0.3	1.2
CaO	55	24.4	31.2	29.5	31	32	3.5	25.1	13.5	22.1
TiO ₂	0.07	0.14	0.12	0.03	0.13	0.10	0.61	0.22	0.4	0.24
MnO	0.03	0.02	0.003	0.06	0.004	0.07	0.06	1.8	0.83	0.1
Fe ₂ O ₃	0.5	0.9	0.07	1.2	0.05	1.9	9.8	6.9	17.2	6.9
Na ₂ O	0.04	0.08	0.13	0.07	0.13	0.05	0.09	0.1	0.09	0.11
LOI	39	36	26	40	27	32	31	20	22	17
Co	13	23	6.5	14	2.4	38.1	92	468	367	52
Ni	1.9	5.5	0.9	7.1	2.2	17.2	991	3267	2278	297
Cu	0.9	0.7	0.8	2.9	0.8	51	461	31.1	19.8	74
Zn	1.7	5	0.4	2.6	0.5	29.1	43	231	336	72
Sr	375	1508	1182	149	175	306	32	719	251	325
Y	1.8	0.6	0.4	0.4	0.4	2	3.1	37	76	8.9
Zr	16.2	24	10	5.6	7.1	11	55.5	16.2	34	26
Pb	4.6	2.1	1.7	1.6	1.6	7.2	3.6	5.6	1.6	3.8
Mo	3.4	2.5	3	5.6	2.7	3.1	2.9	3.3	3.5	3.1
Ba	28.4	285	38	15.9	52.8	97	152	171.2	206	352
U	9.9	7.2	8.4	7.8	7.9	11.2	7.5	10	10	9.5

Sulfur and oxygen stable isotope analyses were performed for samples containing evaporate at the Environmental Isotope Laboratory, Department of Earth Sciences of the University of Arizona. For sulfur isotopes, the Vienna Canon Diablo Troilite (V-CDT) standard was used (absolute isotope ratio $(44360 \pm 40) \times 10^{-6}$) according to [26]. For $\delta^{34}\text{S}$

isotope analysis, 15 samples were weighed twice to 1 mg in 6×4 mm tin capsules, and 0.5 mg vanadium pentoxide was added to them. After this process, the single quartz packed with tungstic oxide and pure copper wires were placed in a Eurovector furnace tube at 102°C , and the burnt gases were analyzed in an IsoPrime isotope ratio mass spectrometer. The $\delta^{18}\text{O}$ isotope was measured on CO gas in a continuous-flow gas-ratio mass spectrometer (Thermo Electron Delta V). A total of seven samples were combusted with excess C at 1350°C using a thermal combustion elemental analyzer (ThermoQuest Finnigan) coupled to the mass spectrometer. The $\delta^{18}\text{O}$ isotope results are presented in this study using the Vienna Standard Mean Ocean Water (V-SMOW) standard with an absolute isotope ratio $(2005.20 \pm 0.45) \times 10^{-6}$, according to [27].

Strontium isotope geochemical experiments were completed on 15 gypsum and anhydrite samples in the Central Laboratory of the Middle East Technical University (METU) (Ankara, Turkey) by applying the Sr isotope ratio analysis experimental instructions adapted from methods with details and conditions given by [28]. The measurements were performed with multiple-collection using a Triton Thermal Ionization Mass Spectrometer (Thermo Fisher Scientific, Waltham, MA, USA). Analytical uncertainty was at 2 sigma level. Samples were first placed in deionized water and dried to almost evaporation after dissolution. Later, the samples were left in 4 mL 14 N HNO_3 for one day and were fully dissolved on a heating table. These samples were dried again almost to evaporation on the heating table, then placed in 1 mL 2.5 N HCl and prepared for chromatography. Strontium was separated in a Teflon column using Bio Rad AG50 W-X8 100–200 mesh resin with 2 mL volume of 2.5 N HCl acid. Strontium was loaded using a Ta-activator on a single Re filament and 0.005 N H_3PO_4 and measured in static mode. The $^{87}\text{Sr}/^{86}\text{Sr}$ data were normalized to $^{86}\text{Sr}/^{88}\text{Sr} = 0.1194$.

4. Results

4.1. Sedimentological Aspects of the Köprübaşı Evaporites

The Köprübaşı evaporites are composed of Ca-sulphate minerals (gypsum and anhydrite). These are occasionally alternated with gray and yellow–beige limestones, gray–black, rough-textured and layered dolomitic limestones, red sandstone and mudstone, and conglomerate and greenish claystone levels (Figure 3a). The evaporitic unit consists of primary selenitic gypsum, gypsarenite, anhydrite, and secondary gypsum formed due to the anhydritization of primary gypsum, and then the hydration of these anhydrites (Figure 3a–l). Secondary gypsums were classified according to their sedimentary structures as massive, satin-spar and laminated (Figure 4a–l).

Massive secondary gypsum can be observed at some levels in cream-yellow, bedded, laminated, undulated and folded, alternating with claystone, sandstone and carbonates levels (Figure 3a,b). These gypsums are homogeneous, white or milky-white in color, very fine-grained alabastrine (Figure 3c), medium to coarse-grained porphyroblastic texture and chicken-wire structures (Figure 3a). These were derived from the re-hydration of anhydrite and contained occasional anhydrite relicts. The satin-spar gypsum observed in fractures and cracks generally develop parallel or semi-parallel to the vein walls and contain fibers varying from a few mm to cm (Figure 3d). There are enterolitic and undulated structures in laminated gypsums and the thicknesses of the laminae vary between 1 mm and 5 mm. (Figure 3e). Selenitic gypsums are between 1 and 15 cm in size, transparent, shiny, white and brown in color and in lensoidal are prismatic, radial and fibrous-fan crystal shapes (Figure 3f–h). Selenitic gypsums are partially anhydritized in some areas (Figure 3g). These are observed in the cracks and cavities of the rocks and as interbands in the rocks (Figure 3i–k). Selenites are altered into anhydrite, then into secondary gypsums during the early–late diagenetic stages. In these selenites, diagenetic alteration intermediate bands Fe-rich intermediate bands are encountered in places (Figure 3k). Gypsarenites are creamy-white, very fine-grained, with ripples, laminated, Fe-oxidized, interbanded and carbonate intercalated (Figure 3l).

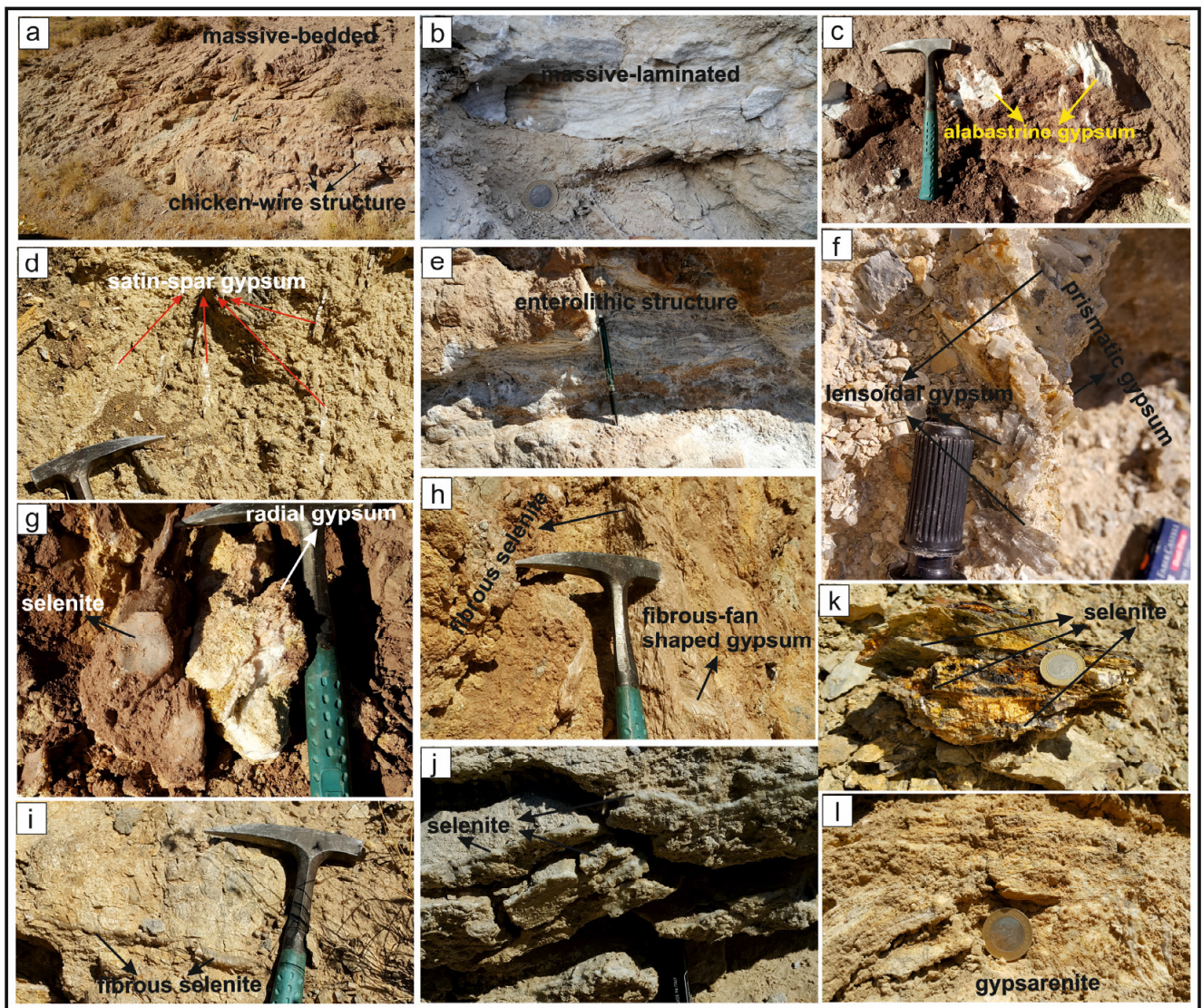


Figure 3. Sedimentologic aspects of the Köprübaşı evaporites. (a) Massive-bedded secondary gypsums with interbedded clay and carbonated and chicken-wire structures; (b) clay laminated-undulated massive secondary gypsum; (c) milky-white color alabastrine massive gypsum in the red-brown mudstone; (d) satin-spar gypsum developing perpendicularly to the vein wall, filling the limestone cracks; (e) undulated-laminated secondary gypsums and enterolithic structures; (f) prismatic-lensoidal selenitic gypsums filling the limestone cracks; (g) euhedral gypsum and partially anhydritized radial selenitic gypsum; (h) fibrous and fibrous-fan shaped selenitic gypsums (some parts partially and completely anhydritized); (i) fibrous selenite within the dolomitic limestone cavities; (j) partly anhydritized selenite interbands in the carbonate rock; (k) selenite interbands containing Fe-oxide and sulfur alteration; (l) gypsarenites anhydritized in some places, containing ripple mark structures.

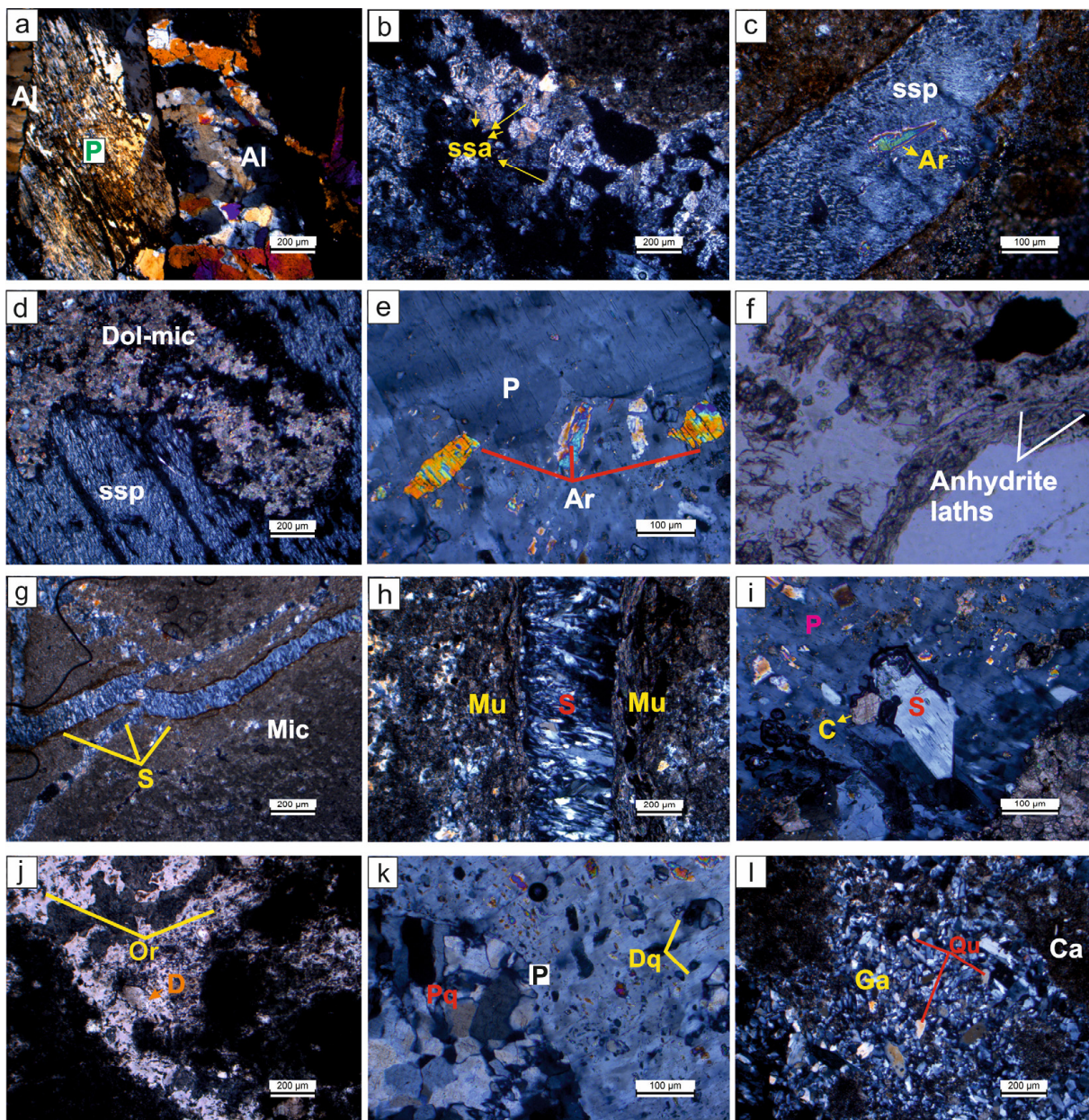


Figure 4. Petrographic images of the evaporitic rock samples. (a) Alabastrine (Al) textured secondary gypsum replacing porphyroblastic (P) gypsum texture (OBK-6-Gönen); (b) spindle-shaped acicular (ssa) crystalline textured secondary gypsums (OBK-18-Gönen sample); (c,d) (ssp) and anhydrite relict (Ar), a specific orientation and carbonation (dolomitic textured) (K-10 Köprüaçzı); (e) subhedral-anhedral anhydrite grains in (P) (OBK-21-Gönen); (f) primary anhydrite laths within the dolomitic mud (Plane light) (K-4 Köprüaçzı); (g) satin-spar gypsum (S) filling cracks within the micritic carbonate (Mic) (B-10 Örencik); (h) muscovite minerals (Mu) observed along the (S) veinlets (K-4 Köprüaçzı); (i) subhedral and euhedral secondary calcite minerals (C) replacing tabular gypsum (Tg) and (P) (OBK-21 Gönen); (j) organic matter relicts (Or) and rhombohedral dolomite (D) (Plane light) (OBK-18 Gönen); (k) detritic (Dq) and polycrystalline quartz (Pq) grains within the (P) (OBK-21 Gönen); (l) gypsarenite (Ga), the cavities of which are filled with quartz (Qu) grains and carbonates (Ca) (OBK-18 Gönen).

4.2. Petrography

The massive gypsums have porphyroblastic (moderate to coarse grained), alabastrine (fine grained), micritic (calcite grains < 4 µm) and dolomitic textures (Figure 4a–g).

Alabastrine and porphyroblastic secondary gypsum textures are observed together in some samples (Figure 4a). While porphyroblastic texture has clear boundaries, alabastrine texture has no clear boundaries (Figure 4a). These porphyroblastic gypsums exhibit spindle-shaped acicular crystalline and spindle-shaped parallel crystalline textures as they undergo alteration along their cleavage surface during the late stages of diagenesis (Figure 4b–d). In addition, a certain orientation and folding is observed in the porphyroblastic gypsum, which are affected by tectonism in the environment (Figure 4d). This gypsum is exposed to carbonatization along its long axis, and dolomite and quartz crystals replace these gypsums during the late diagenetic stage. Additionally, they contain anhydrite relicts (Figure 4e). These anhydrite crystals are sometimes observed growing displaced, between 0.3 mm and 4 mm in size and primarily prismatic lath-shaped within the dolomitic mud (Figure 4f).

Satin-spar gypsums form as parallel fibers and are perpendicular to the long axes of fractures and cracks of micritic textured rocks (Figure 4g). In some thin sections, severed muscovite and sericite minerals of the Bitlis metamorphics are observed along the satin-spar gypsum veinlets (Figure 4h). These minerals generally extend in orientation with satin-spar gypsum. Sometimes, the grains of these metamorphics are scattered in the gypsum. Euhedral and anhedral calcite crystals are observed within these secondary gypsums (Figure 4i). Organic matter relicts, rhombohedral dolomite mineral, Fe-oxide alteration (Figure 4j), sometimes as detrital or syn-sedimentary polycrystalline quartz grains, are observed in some samples (Figure 4k). These dolomite minerals replaced porphyroblastic gypsum in the late diagenetic phase.

Selenitic gypsum shows first order interference colors with a grain size of up to 4 mm, with distinct unidirectional cleavage traces (Figure 4i). Simple twinning and fractures are frequently observed and are replaced by late diagenetic calcite minerals. Additionally, tabular gypsums have anhydrite relicts (Figure 4i). The gypsarenites have grains the size of sand and the spaces between the grains are observed to be filled with carbonate or clay cement and detrital material (Figure 4l).

4.3. Mineralogy

According to XRD analysis, the main mineral in Köprüağzı (K), Örenkale (O), Örencik (B) and Gönen (OBK) evaporitic samples is gypsum, and other accompanying minerals are anhydrite, calcite, dolomite, quartz, chlorite, kutnohorite and plagioclase (Figure 5a–f). Gypsum ($\text{CaSO}_4 \cdot 2\text{H}_2\text{O}$), anhydrite (CaSO_4), celestine (SrSO_4), calcite (CaCO_3), dolomite (Ca-Mg carbonate) and some iron, clay and siliciclastic minerals were determined in the SEM analysis.

Calcite and dolomite exhibit prismatic or rhombohedral morphologies (Figure 6a). Anhydrite laths and celestine are encountered in the secondary gypsum (6b). In gypsum samples, high rates of hematite or magnetite type Fe oxidation zones, sulfidation and microbial-derived framboidal pyritization are common (Figure 6c,d). The grain size of framboidal pyrites are generally smaller than one micron and contain equidimensional, spherical to semi-spherical or polyframboidal morphology and clusters of microcrystals (Figure 6c). The Mg-rich clay minerals (sepiolite, saponite and palygorskite), quartz and potassium feldspar are emplaced along fractures of tabular and hemi prismatic gypsums (Figure 6d). These clay minerals have a fine-grained, plated and occasionally honeycomb appearance with grain size up to 10 microns (Figure 6c,d). We observed good cleavage in prismatic-tabular gypsum crystals, though occasional deformation structures were observed (Figure 6d). Additionally, orthorhombic anhydrite, K-feldspar and quartz minerals were detected (Figure 6e,f).

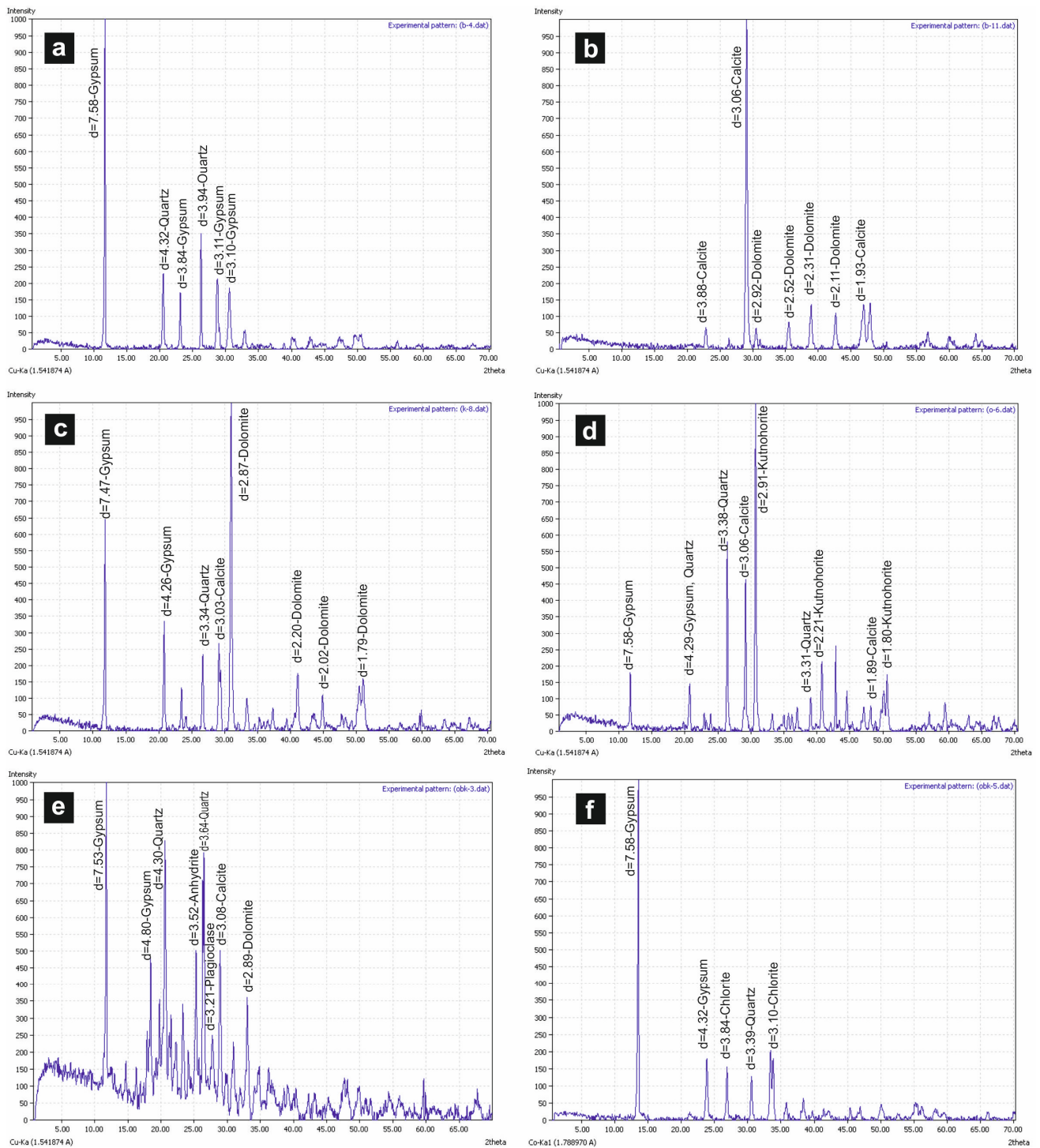


Figure 5. (a,b) XRD peaks of B-4 and B-12 samples (Örencik); (c) XRD peaks of K-8 sample (Köprüağzı); (d) XRD peaks of O-6 sample (Örenkale); (e,f) XRD peaks of OBK-4 and OBK-15 samples (Gönen).

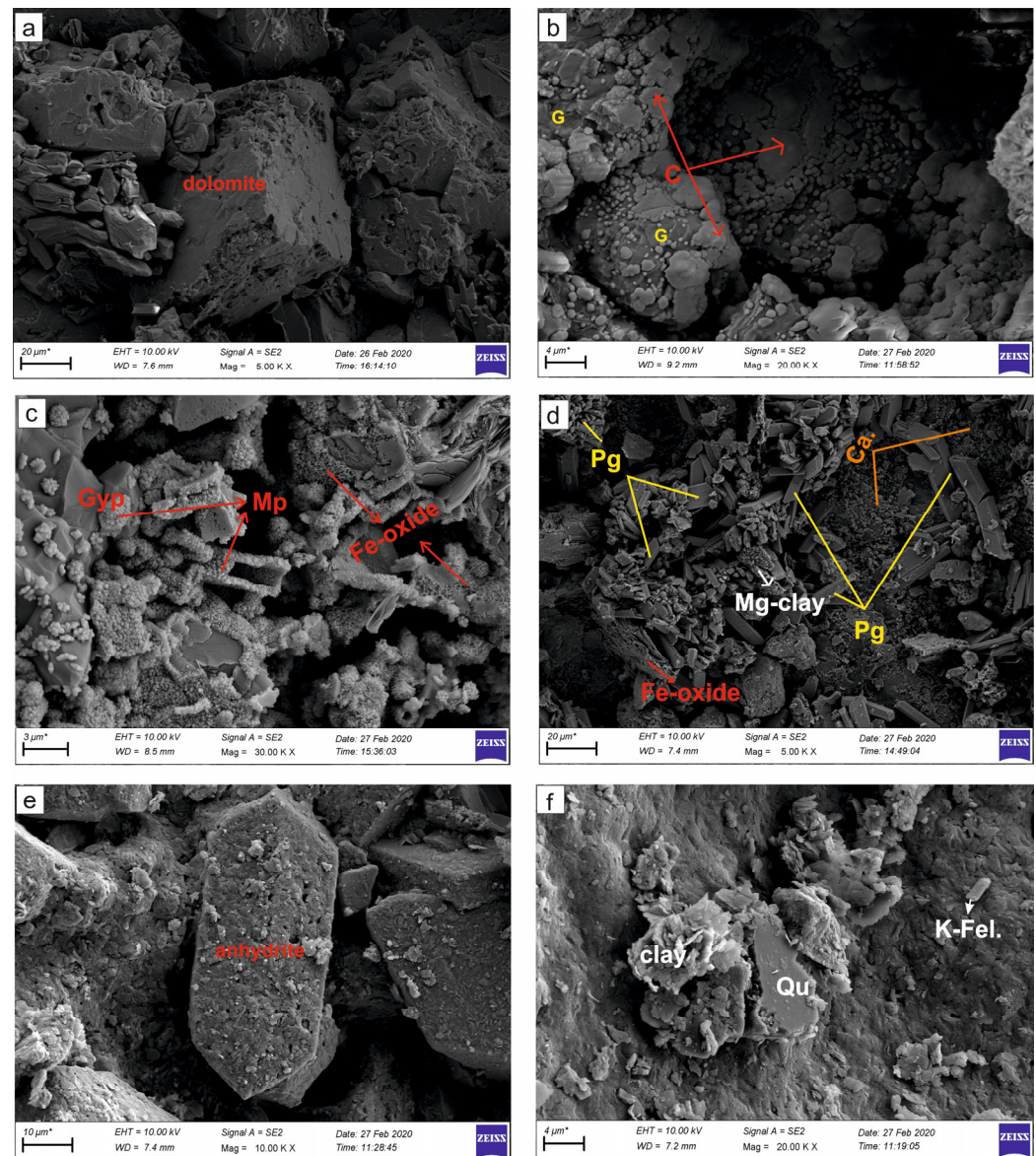


Figure 6. SEM images of the evaporitic rock samples. (a) Euhedral semi-euhedral rhombohedral dolomite minerals in massive-laminated gypsum (K-11 Köprüağzı); (b) the nodular-shaped celestine (C) replacing secondary gypsum (G) (OBK-5 Gönen); (c) microbial pyrite (Mp) formations and Fe-oxidation in the gypsum (Gyp) (K-5 Köprüağzı); (d) the plate-like formed Mg-rich clay minerals, Fe-oxide and carbonatization (Ca.) areas in the prismatic gypsum (Pg) (O-6 Örenkale); (e) orthorhombic prismatic anhydrite (Anh) crystal; (f) Mg-rich clay, quartz (Qu) and potassium feldspar (K Fel.) minerals in gypsum (O-6 Örenkale).

4.4. Element Geochemistry

In gypsum samples, positive correlations between SiO_2 with Al_2O_3 were observed ($r = +0.91$ for B, K and O samples), MnO ($r = +0.26$), Fe_2O_3 ($r = 0.91$ for B, K and O samples; $r = +0.98$ for OBK samples), MgO ($r = +0.53$), TiO_2 ($r = +0.35$ for OBK samples) and P_2O_5 ($r = +0.30$ for OBK samples) (Figure 7). While the SiO_2 , Al_2O_3 and CaO values were observed to be very high in all samples, the Na_2O , MgO , P_2O_5 , K_2O , MnO and TiO_2 concentrations were very low compared with these (Table 1). There were negative correlations between SiO_2 and CaO ($r = -0.27$ for B, K and O samples; $r = -0.40$ for OBK samples) and SO_3 ($r = -0.52$ for B, K and O samples; $r = -0.89$ for OBK samples) (Figure 7). There were negative and positive trends between $\text{Na}_2\text{O}-\text{Al}_2\text{O}_3$ ($r = -0.53$), $\text{Na}_2\text{O}-\text{K}_2\text{O}$ ($r = -0.67$) and $\text{Na}_2\text{O}-\text{TiO}_2$ ($r = +0.53$) (B, K and O samples), respectively (Figure 7). Most gypsums contained very high

concentrations of trace elements (such as Co, Ni, Cu, Zn, As, Rb, Zr and Y) (Table 1). Ba (up to nearly 350 ppm) and Sr (up to 1508 ppm) trace element concentrations were high in gypsum samples. The OBK-3 sample of the Gönen section was differentiated from other samples by low Sr trace element content (32 ppm) (Table 1). There was a positive trend ($r = 0.98$) between Ni and Co elements, while Sr/Ba had a negative trend (-0.58) with Al_2O_3 (Figure 7). Gypsum samples presented high values for Fe_2O_3/MnO (mean 37), Zr/Al_2O_3 (mean 94), Sr/CaO (mean 20), Ni/Co (up to 11), Co/Zn (up to 16), Sr/Ba (up to 32) and Cu/Zn ratios (up to 11) (Table 1). Additionally, a high positive correlation (Figure 7) between Ni with Co ($r = +0.91$ for B, K and O samples; $r = +0.98$ for OBK samples), Ba with Sr ($r = +0.70$ for B, K and O samples) and Cu with Zn ($r = +0.98$ for B, K and O samples) (Figure 7) was observed.

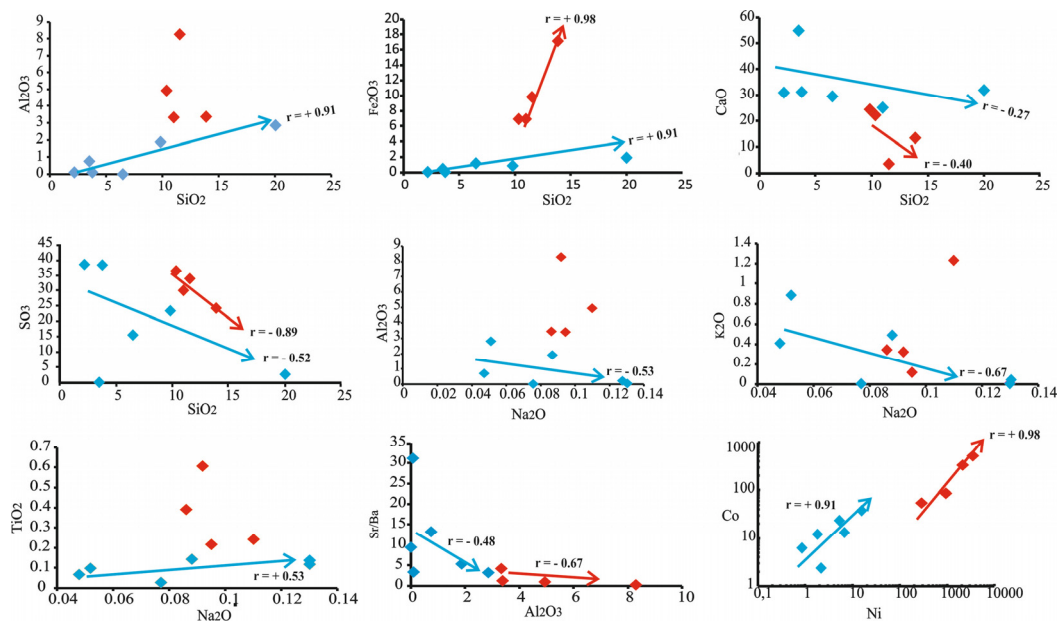


Figure 7. The variation diagrams between major oxides and trace elements of the evaporate rock samples (blue boxes show samples B-7-11, K-5-8-12, and O-6, while red boxes show samples OBK-3-4-6-7).

4.5. Isotope Geochemistry

A total of fifteen evaporite samples were selected for $^{87}Sr/^{86}Sr$ and $\delta^{34}S$ isotope analyses (Table 2). The $^{87}Sr/^{86}Sr$, $\delta^{18}O$ (seven samples) and $\delta^{34}S$ isotope values vary between 0.707769 and 0.709098, 12.1 to 14.7‰ and 5.8 to 34.5‰, respectively (Table 2).

Table 2. Isotope values ($\delta^{34}S$, $\delta^{18}O$ and $^{87}Sr/^{86}Sr$) of different evaporite rock samples intercalated with clay-carbonate.

Sulfate Samples	Sample No	$\delta^{34}S$ (CDT)	$\delta^{18}O$ (SMOW)	$^{87}Sr/^{86}Sr$
Alabastrine gypsum	K-3	34.5	13.8	0.7087
Anhydritized selenite	K-5	34.2	14.1	0.7088
Anhydritized gypsarenite	K-8	31.6		0.7085
Undulted-laminated	K-9	30.3	14.7	0.7084
Porphyroblastic gypsum	K-11	30.5	13.6	0.7086
Lensoidal gypsum	B-4	30.6		0.7089
Massive-laminated gypsum	B-7	30.4	12.1	0.7088

Table 2. Cont.

Sulfate Samples	Sample No	$\delta^{34}\text{S}$ (CDT)	$\delta^{18}\text{O}$ (SMOW)	$^{87}\text{Sr}/^{86}\text{Sr}$
Anhydrite	B-12	30.1		0.7089
Porphyroblastic gypsum	B-15	29.9	13.1	0.7087
Anhydritized tabular gypsum	O-1	28.1		0.7090
Massive	O-6	26.6		0.7091
Anhydrite	O-13	27.8	14.8	0.7089
Satin-spar gypsum included carbonate	OBK-4	6.9		0.7078
Laminated gypsum included clayey carbonate	OBK-7	5.8		0.7078
Laminated gypsarenite	OBK-15	30.3		0.7086

5. Discussion

5.1. Paleoenvironmental Conditions

5.1.1. Sedimentological—Petrographical Interpretation

The paleo depositional conditions and sedimentary model for gypsum-rich succession in the Başkale Basin was interpreted based on element concentrations, sedimentological, petrographical—mineralogical and elemental analyses parameters. Some gypsum lithofacies and sedimentary structures in the basin may provide evidence about paleo depositional environment. The observation of massive gypsum lithofacies in the study area, which contain laminations, reflects a saline depositional environment with shallow or moderate depths, e.g., [29,30]. Massive secondary gypsums are formed by primary gypsum (selenitic and gypsum arenitic) losing water due to the increase in salinity during the early diagenetic stages to become anhydrite (see Figure 4i,l). During the late diagenetic phase, the secondary gypsums (alabastrine and porphyroblastic) (see Figure 4a–e) are formed as a result of the reaction of anhydrite, which uplifts with the effect of tectonism or lithostatic pressure, with meteoric or groundwater. The observation of these two secondary gypsums together indicate that the dissolution–recrystallization processes were developed (see Figure 4a). Since these porphyroblastic and alabastrine textured gypsums were altered along the cleavage surfaces during the late diagenesis, they showed spindle-shaped acicular crystal and spindle-shaped parallel crystal textures (see Figure 4c,d). The folds and orientations were sometimes observed in these, due to the effect of tectonism in the region. Additionally, the presence of fine-grained primary gypsums (lensoidal, tabular, etc.) crystallizing in the cracks and cavities of the rocks support these processes. These freely-growing and crack-filling gypsums were formed by the rise of the humic acid and/or sulfate-rich groundwater level and the increase in the evaporation rate. Since their crystallization is quite rapid, they are observed as relatively smaller crystals in cracks [31]. These type of gypsums reflect coastal areas where lake water retreats. Anhydrite relicts in secondary gypsums prove that the mineral formed before these during the early–late diagenesis was anhydrite (see Figure 4c,e). Additionally, the anhydrite relicts in the secondary gypsums were formed by preserving the tabular gypsum frame, indicating that these secondary gypsums were derived from primary gypsum (Figure 5i). Calcite and dolomite minerals replaced secondary gypsums during the late diagenetic stage with the input of carbonate-rich groundwater (see Figure 4d,i). These massive secondary gypsums that generally alternated with dolomitic limestone levels indicate the lagoon environment and increased salinity [32,33]. The presence of anhydrite laths in dolomitic mud in the samples taken from the Köprüağzı (K) and Örencik (B) sections confirms that these anhydrites were formed during the sedimentation (Figure 4f), e.g., [34]. No microscopic or macroscopic evidence was found that secondary gypsum was derived from these primary anhydrites in the study area (e.g., nodular gypsum/anhydrite).

The greenish claystones alternating with some gypsum lithofacies (satin-spar and anhydritized gypsum, etc.) show short-term playa waters after the lagoon [29] and low-

energy depositional conditions [35,36]. Further proof of this is the limited lateral continuity of the laminated gypsum in the field. Volume changes as a result of regional tectonics or during the gypsum–anhydrite transformation formed enterolitic folds (see Figure 4e) in the laminated gypsum [37]. Likewise, secondary satin-spar gypsums were formed in the cracks caused by the volume changes created by these mineral transformations during the late diagenesis (Figures 3d and 4g). These structures also document the existence of the coastal sabkha mud flats environments, which are further inland [38,39]. Additionally, the gypsarenite and selenitic gypsum lithofacies in this study area also support the shallow-water depositional environment [40].

5.1.2. Mineralogical Interpretation

The presence of primary gypsum crystals such as prismatic, tabular and lenticular with smooth surfaces (Figures 4i and 6d), twinning and cleavage surfaces in the field indicates that environmental conditions such as pH, temperature and salinity are gradually increasing [41]. However, the presence of kutnohorite mineral in gypsum identified by XRD (Figure 5d) and observation of framboidal pyrite identified in SEM studies (Figure 6c) indicate low [42] and neutral pH conditions in the environment [43], respectively. Therefore, pH conditions were continuously changed in the study area. With these minerals, dark brown colors in primary gypsum and organic matter relicts (see Figure 4j) in thin sections indicate the presence of organic matter activity and anoxic conditions [42,44]. The development of intermediate bands rich in Fe oxide in primary gypsum (in both field and SEM-EDS analysis) (Figures 3k and 6c,d) shows the effect of hydrothermal solutions developed due to Neogene–Quaternary volcanism in the region or freshwaters eluviation from the surrounding basaltic rocks [45]. Celestine is formed by the replacement of Ca in gypsum by Sr (hydrothermal solution originated). Therefore, in the SEM study, the detected celestine in gypsums supports the existence of these hydrothermal solutions [46,47].

5.1.3. Elemental Analyses Interpretation

In SiO₂ versus major oxides variation diagrams, MnO ($r = +0.26$), Fe₂O₃, MgO, TiO₂ and P₂O₅ exhibit positive trends (Figure 7). This indicates that the paleo depositional environment was shallowed due to evaporation and clay or clastic (especially siliciclastic) materials were transported into the region from continental sources [48,49]. The very high SiO₂ concentrations in our samples, a negative correlation of SiO₂ with CaO and SO₃ (Figure 7), high Zr values and Zr/Al₂O₃ ratio (Table 1) and quartz, feldspar, zircon, chlorite and smectite group clay minerals identified in mineralogical studies also support the intense detrital material input into the basin [50]. Interlocked polycrystalline quartz grains observed, especially in petrographical and mineralogical studies, are characteristic of clastic quartz from a metamorphic source (Bitlis Massif) and are transported by surface waters [51] (Figures 4k and 6f). Similarly, plagioclase and K-feldspar minerals were transported into the basin in this system.

The content of metallic elements such as Ni (up to 3267 ppm), Cu (up to 461 ppm), Co (up to 468 ppm), Zn (up to 335 ppm) and Pb (up to 7.2 ppm) (Table 1) can also be attributed to the clastic material input derived from ultramafics of the Yüksekova Complex. In addition, these clay minerals represent humid climatic and alkaline environmental conditions [52–56].

It shows negative correlations with Na₂O, Al₂O₃ and K₂O and positive correlation with TiO₂. These correlations indicate high chemical weathering and humid climate conditions in the environment, e.g., [57] (Figure 7). Sr contains values between 1000 and 3000 ppm in marine environments [58,59] and 50–200 ppm in continental environments [60]. The studied samples were below these values except for two samples (B-7 and K-12). These low values (Table 1) reflect the mixing seawater and non-marine fluids and the presence of dissolution–reprecipitation processes [47,61–63]. Additionally, Sr and Ba contents and the negative trend of Sr/Ba with Al₂O₃ ($r = -0.48$ for B, K and O samples; $r = -0.67$ for OBK samples) (Figure 7) and Sr/Ba, Sr/CaO and Fe₂O₃/MnO ratios show salinity increased

in the depositional environment [64,65]. Some element contents in the studied gypsum samples reflect organic matter activity, high salinity and reducing conditions within the gypsum (U, Mo, Ni, Cu and Zn and Co, Ni/Co, Co/Zn and Cu/Zn ratios), e.g., [66–72]. Moreover, the high positive correlation (Figure 7) between Ni with Co, Ba with Sr and Cu with Zn emphasizes a continental source [73].

5.2. Origin, Age and Source of the Köprüağzı Evaporites

Investigation of $^{87}\text{Sr}/^{86}\text{Sr}$, $\delta^{34}\text{S}$ and $\delta^{18}\text{O}$ ratios undertakes an effective role in understanding the depositional age, marine or non-marine origin and source of the evaporites [74,75]. In transitional environments (such as coastal sabkha and lagoon), different contributions (e.g., groundwater, presence of celestine, hydrothermal fluids, diagenetic solutions and sulfate-reducing bacteria) affect strontium and sulphate isotopes and may provide different isotopic signals causing confusion in source interpretations [76].

Sr isotope ratios of the Köprüağzı evaporites (0.708444–0.709098) (except OBK-4 and OBK-7 samples) (Table 2) indicate Cambrian marine sulfates ratios 0.7081–0.7093; [77–80] (Figure 8a). The sharp decrease in $^{87}\text{Sr}/^{86}\text{Sr}$ isotope values in OBK-4 (0.707765) and OBK-7 (0.707769) samples can be attributed to hydrothermal or freshwater inputs, e.g., [79,81–83]. The $\delta^{34}\text{S}$ ratios ranging from 28‰ to 38‰ indicate the Cambrian age [84–88] and marine sulfate origin [89,90]. The Köprüağzı evaporites' $\delta^{34}\text{S}$ isotope ratios (average 30.3‰) are compatible with Cambrian marine sulfates, as in Sr isotopes (Figure 8b). In addition, these values indicate that the source of sulfur dissolved in sulfates in the study area was the isotope fraction during bacterial sulfate reduction in hypersaline and partial anoxic environments, e.g., [47,89,91]. Furthermore, the sharp decrease in the sulfur isotope values of OBK-4 and OBK-7 samples may be due to the mixing of sea water with rivers and hydrothermal temperatures [47] at these levels of the sequence. The $\delta^{18}\text{O}$ isotope values (average 13.89‰) in the studied evaporites were also consistent with the oxygen isotope values of the Cambrian marine sulfates' average of 13.74‰ [85].

The Köprüağzı evaporites stratigraphically overlie the metamorphics of the Bitlis Massif (Precambrian—Paleozoic) [92] and contain blocks belonging to this massif in the lower parts (Figure 2a). It is overlain by the Yüksekova Complex with tectonic contact (Figure 2a,e). Blocks of this complex are observed in the upper parts of the evaporites (Figure 2a,b). Additionally, many Cambrian marine evaporites are known to exist in Iran along the BZSZ [18,93–99] (Figure 9f).

Considering the stratigraphic position of Köprüağzı evaporites, it seems that these evaporites were carried over the Bitlis Massif by tectonic movements. The blocks belonging to the Massif and Complex in the evaporites prove this transportation. Therefore, these evaporites must be younger than the Bitlis Massif and the Yüksekova Complex. This shows that the evaporites cannot be of Cambrian age. At the same time, the most of the studies conducted in Iran discuss the halokinetic phases and remobilization of salt deposits via salt tectonics. Thus, the evaporites in the study area are genetically different from the Cambrian evaporites in Iran. This supports that the Köprüağzı evaporites cannot be Cambrian.

Some studies have been carried out on the existence of Triassic “Marble Rosetta” in the Bitlis Massif of the Alanya-Bitlis block [100–102]. They stated that Rosetta Marble was formed after large primary selenite crystals underwent high-pressure low-temperature metamorphism and represented carbonate pseudomorphs. It can be thought that the evaporites in the study area are similar in origin to these evaporites. However, isotope values, sedimentological, petrographic and mineralogical findings show that Köprüağzı evaporites did not undergo metamorphism (no metamorphic texture or mineral could be detected), but only underwent early–late diagenesis processes, and therefore they are not similar with Triassic Rosette Marbles. There are many Miocene evaporite successions in Eastern Anatolia and Iran [103–123] (Figure 9a–e,g–j).

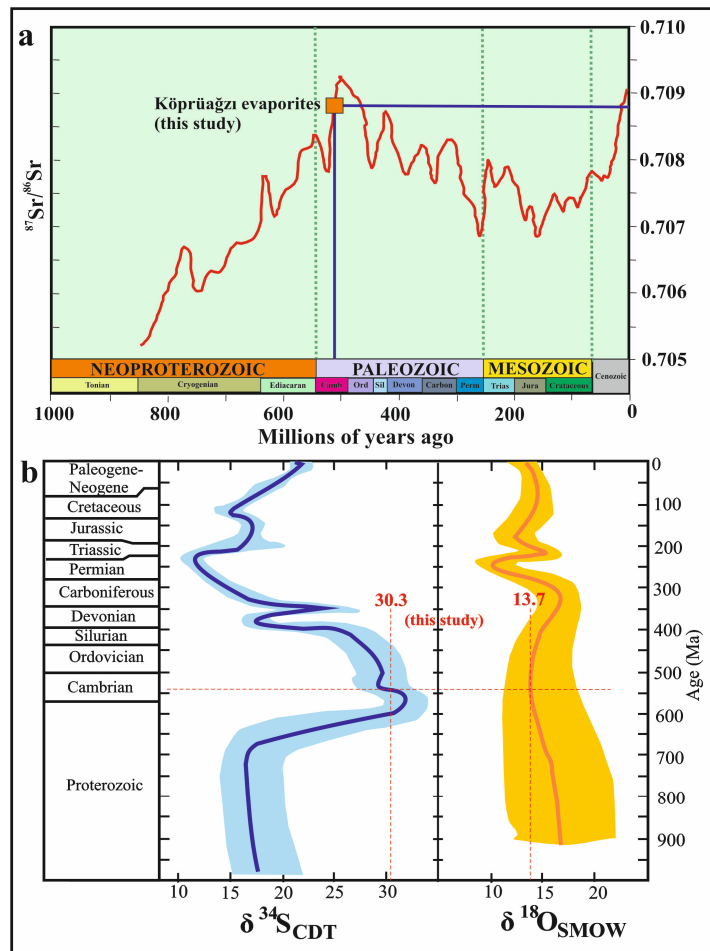


Figure 8. (a) $^{87}/^{86}\text{Sr}$ isotopic curve of seawater strontium during the latest 1000 Ma interval (modified from [77,78,80]); (b) marine sulfate sulfur and oxygen isotope age curves (modified from [85]). The bold line is their best estimate of global oceanic sulfur and oxygen isotope compositions and the shaded area shows an estimate of uncertainty for the curve. The point where the red dashed lines intersect belongs to the study area samples.

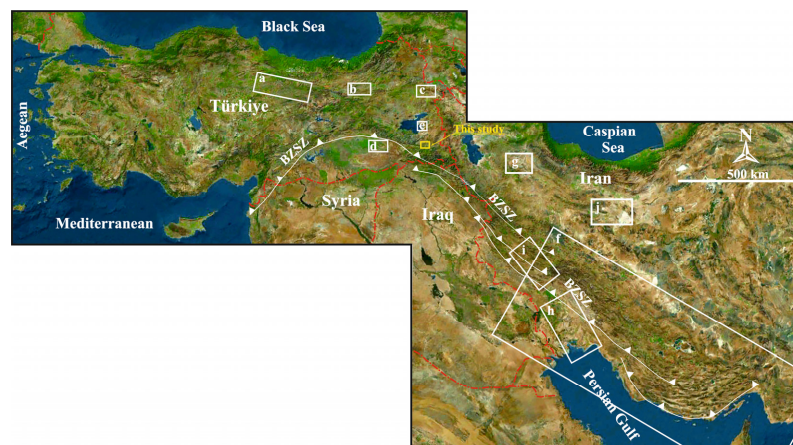


Figure 9. Relief map showing (a–e) Miocene evaporite fields in eastern Turkey, (f) Cambrian evaporite fields deposited along the Bitlis–Zagros Suture Zone (south–southeast Iran) and (g–j) Miocene evaporite fields in Iran. The boxes and the letters inside of them show the previous work in that area. (a): [103,113,115,116,119], (b): [123], (c): [106,107,117,122], (d): [109–111,118–120], (e): [121], (f): [18,93–99], (g): [104], (h): [114], (i): [108], (j): [105].

The $^{87}\text{Sr}/^{86}\text{Sr}$ values between 0.7084 and 0.7089 [78,124] and the $\delta^{18}\text{O}$ values between 13‰ and 14‰ [125] indicate Miocene marine sulfates. While the $^{87}\text{Sr}/^{86}\text{Sr}$ values (0.7088) and the $\delta^{18}\text{O}$ isotope values (13.74‰) in the Köprübaşı evaporites are within Miocene marine sulfate values (Figure 10a,b), the $\delta^{34}\text{S}$ isotope ratios (average 30.3‰) are higher than Miocene marine sulfate values 20‰ [126]. These high sulfur isotope ratios may be due to the bacterial sulfate reduction [127–130]. Additionally, evaporites are located in a very tectonically active region. Therefore, the units have lost their original stratigraphic position. If the Köprübaşı evaporites are Miocene in age, their stratigraphic position can be explained by the collision (Arabian—Anatolian plates) that took place in the region during the Miocene. These evaporites may have been pushed over the Bitlis Massif with the movement of the Yüksekova Complex and gained their recent position. The Massif and Complex blocks in the Köprübaşı evaporites suggest such a scenario (see Figure 2a–e). Additionally, both some mineral orientations in thin sections and folds and undulation structures in the field support this tectonic transport (deformation).

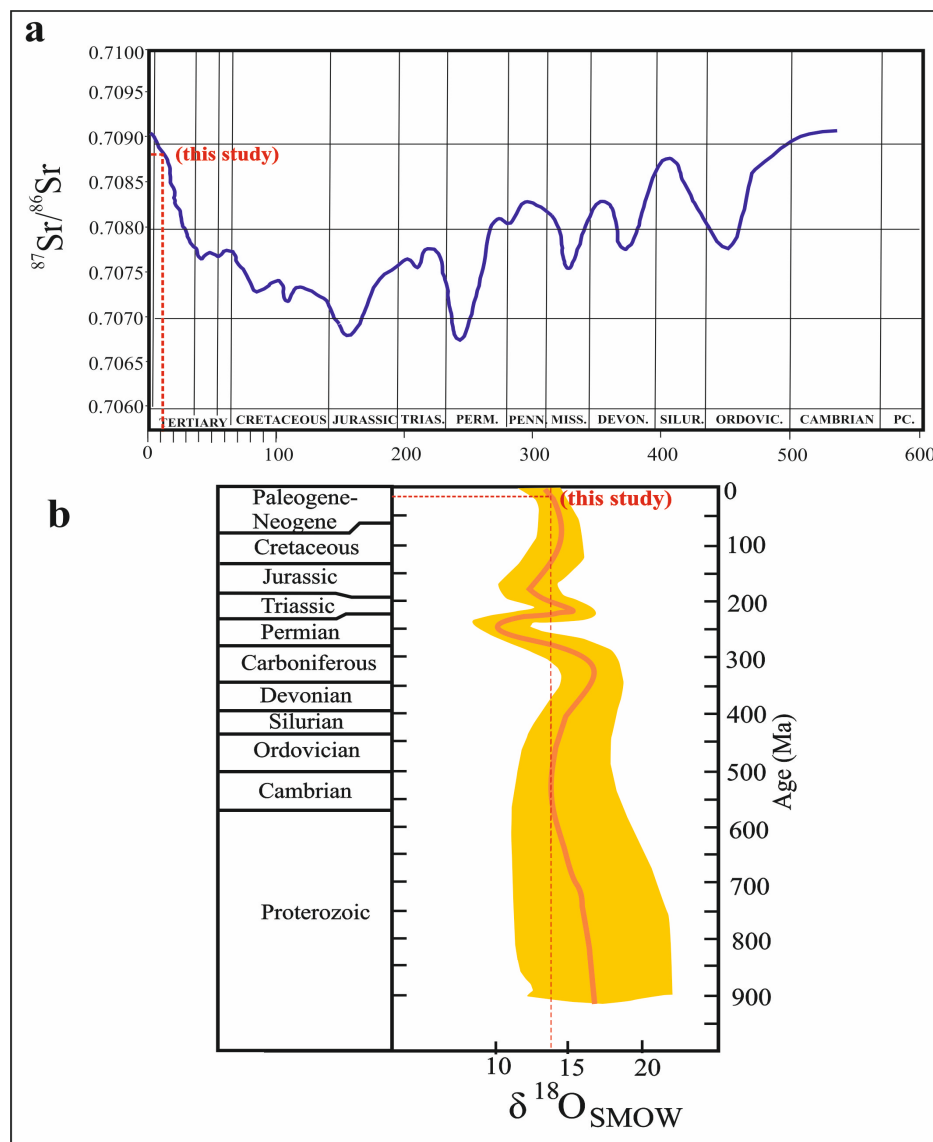


Figure 10. (a) $^{87}\text{Sr}/^{86}\text{Sr}$ isotopic curve of seawater strontium during the latest 1000 Ma interval [78]; (b) marine sulfate sulfur and oxygen isotope age curves (modified from [85]).

6. Conclusions

The $^{87}\text{Sr}/^{86}\text{Sr}$ isotopic ratios and $\delta^{34}\text{S}$ -CDT and $\delta^{18}\text{O}$ values for the Köprübaşı evaporites indicate that these evaporites formed in a Miocene marine origin. The evaporites were deposited in an area extending from lagoon to its hinterland. Sedimentological and petrographical-mineralogical findings indicated that these evaporites were composed of primary and secondary gypsum, and secondary gypsum (alabastrine massive, laminated gypsum, satin spar gypsum, etc.) was derived from primary gypsum (selenite and gysarenite) during the early and late diagenetic processes. Additionally, sedimentological, mineralogical and geochemical studies revealed increased salinity, reduction conditions, fluctuations in pH values, fluvial and hydrothermal effects and associated dense clastic material inflows and organic matter activity in a basin under a dry–humid climate, tectonism and diagenetic effects. **Author Contributions:** Methodology and field studies, P.G.Y. and O.B.;

laboratory studies and interpretation, P.G.Y.; writing and editing, P.G.Y. All authors have read and agreed to the published version of the manuscript.

Funding: This study was supported by the Van Yüzüncü Yıl University Scientific Research Projects Coordination Unit, Project No: FYL-2019-8257).

Data Availability Statement: Not applicable.

Acknowledgments: This work is a part Ozan Baran's master's dissertation, which will be submitted to the Department of Geology, Faculty of Engineering, Van Yüzüncü Yıl University of Turkey.

Conflicts of Interest: The authors declare no conflict of interest.

References

- Warren, J.K. *Evaporites: A Geological Compendium*, 2nd ed.; Springer: Berlin/Heidelberg, Germany, 2016.
- Bukowski, K.; Czapowski, G.; Karoli, S.; Babel, M. Sedimentology and geochemistry of the Middle Miocene (Badenian) salt-bearing succession from East Slovakian Basin (Zbudza Formation). *Geol. Soc. Lond. Spec. Publ.* **2007**, *285*, 247–264. [[CrossRef](#)]
- Şengör, A.M.C.; Yılmaz, Y. Tethyan evolution of Turkey: A plate tectonic approach. *Tectonophysics* **1981**, *75*, 181–241. [[CrossRef](#)]
- Koçyiğit, A.; Yılmaz, A.; Adamia, S.; Kuloshvili, S. Neotectonics of East Anatolian Plateau (Turkey) and Lesser Caucasus. Implication for transition from thrusting to strike-slip faulting. *Geodin. Acta* **2001**, *14*, 177–195. [[CrossRef](#)]
- Şaroğlu, F.; Yılmaz, Y. Doğu Anadolu'da Neotektoniğin jeolojik gelişime başlıca etkileri. *Bull. Miner. Res. Explor.* **1986**, *107*, 73–94.
- Şengör, A.M.C. *Turkey'nin neotektoniğinin esasları*, 1st ed.; Turkey Jeoloji Kurumu: Ankara, Turkey, 1980; 40p.
- Koçyiğit, A. *Sütlüce (Hakkâri) Depreminin Kaynağı: (Başkale fay Kuşağı, GD Turkey)*; Deprem Sempozyumu, Kocaeli, 23–25 Mart; Koceli Üniversitesi: Kocaeli, Turkey.
- Acarlar, M.; Türkecan, A. *Başkale (Van) Batı-Kuzeybatısının Jeolojisi*, 1st ed.; Min. Res. Exp.: Ankara, Turkey, 1986; 87p.
- Çevikbaş, A. *Başkale (Van) Yöresinin Jeolojisi*, 1st ed.; Min. Res. Exp.: Ankara, Turkey, 1986; 70p.
- Perinçek, D. Hakkâri İli ve dolayının stratigrafisi (Güneydoğu Anadolu-Turkey). *Turkey Pet. Jeologları Derneği Bülteni* **1990**, *2*, 21–68.
- Şen, A.M.; Bilgin, Z.A.; Erkal, T.; Elibol, E.; Güner, E.; Hakyemez, H.Y.; Gedik, İ.; Uğuz, M.F.; Acarlar, M.; Umut, M. *Van Gölü Doğu ve Kuzeyinin Jeolojisi*, 1st ed.; Min. Res. Exp.: Ankara, Turkey, 1991; 82p.
- Şenel, M. *1:100.000 ölçekli Turkey Jeoloji Haritaları, Hakkâri M51 Paftası*, 1st ed.; Min. Res. Exp.: Ankara, Turkey, 2007; 55p.
- Sağlam Selçuk, A.; Düzgün, M. Başkale Fay Zonu'nun tektonik jeomorfolojisi. *Bull. Miner. Res. Explor.* **2017**, *155*, 33–47.
- Şengör, A.C.; Özeren, S.; Genç, T.; Zor, E. East Anatolian high plateau as a mantle-supported, north-south shortened domal structure. *Geophys. Res. Lett.* **2003**, *30*, 1–4. [[CrossRef](#)]
- Açlan, M.; Altun, Y. Syn-collisional I-type Esenköy Pluton (Eastern Anatolia-Turkey): An indication for collision between Arabian and Eurasian plates. *J. Afr. Earth Sci.* **2018**, *142*, 1–11. [[CrossRef](#)]
- Topuz, G.; Candan, O.; Zack, T.; Yılmaz, A. East Anatolian plateau constructed over a continental basement: No evidence for the East Anatolian accretionary complex. *Geology* **2017**, *45*, 791–794. [[CrossRef](#)]
- Topuz, G.; Altherr, R.; Schwarz, W.H.; Dokuz, A.; Meyer, H.P. Variscan amphibolite facies rocks from the Kurtoğlu metamorphic complex, Gümüşhane area, eastern Pontides Turkey. *Int. J. Earth Sci.* **2007**, *96*, 861–873. [[CrossRef](#)]
- Berberian, M.; King, G.C.P. Towards a paleogeography and tectonic evolution of Iran. *Can. J. Earth Sci.* **1981**, *18*, 210–265. [[CrossRef](#)]
- Yılmaz, A.; Yazgan, E. Structural evolution of the eastern Taurus in the Cretaceous-Tertiary Period. In Proceedings of the International Earth Sciences Colloquium on the Aegean Regions, İzmir, Turkey, 1990.
- Ternek, Z. Van Gölü güneydoğu bölgesinin jeolojisi. *TJK Bull.* **1953**, *4*, 1–27.
- Yılmaz, O. Cacas bölgesi (Bitlis Masifi) kayaçlarının petrografik ve stratigrafik incelenmesi. *TJK Bull.* **1975**, *18*, 33–41.
- Ustaömer, P.A.; Ustaömer, T.; Collins, A.S.; Robertson, A.H.F. Cadomian (Ediacaran–Cambrian) arc magmatism in the Bitlis Massif, SE Turkey: Magmatism along the developing northern margin of Gondwana. *Tectonophysics* **2009**, *473*, 99–112. [[CrossRef](#)]

23. Yılmaz, O. Etude Petrographique et Geochronologique de la Region de Cacas. Ph.D. Thesis, Universite Scientifique et Médicale de Grenoble, La Tronche, France, 1971; 225p.
24. Genç, S. Petrography, metamorphism and genesis of metamorphics in the Çökekyazı Gökay (Hizan, Bitlis) area of the Bitlis massif. *Turkey Geol. Bülteni* **1990**, *33*, 1–14.
25. Norrish, K.; Chappel, B.W. X-ray fluorescence spectrometry. In *Physical Methods in Determinative Mineralogy*; Zussman, J., Ed.; Academic Press: Cambridge, MA, USA, 1977; pp. 201–272.
26. MacNamara, J.; Thode, H.G. Comparison of the isotopic composition of terrestrial and meteoritic sulfur. *Phys. Rev.* **1950**, *78*, 307–308. [[CrossRef](#)]
27. Baertschi, P. Absolute ¹⁸O content of Standard Mean Ocean Water. *Earth Planet. Sci. Lett.* **1976**, *31*, 341. [[CrossRef](#)]
28. Köksal, S.; Toksoy-Köksal, F.; Gönçüoğlu, M.C. Petrogenesis and geodynamics of plagiogranites from Central Turkey (Ekecik-dağ/Aksaray): New geochemical and isotopic data for generation in an arc basin system within the northern branch of Neotethys. *Int. J. Earth Sci.* **2017**, *106*, 1181–1203. [[CrossRef](#)]
29. Schreiber, B.C.; Freidman, G.M.; Decima, A.; Schreiber, E. Depositional environments of Upper Miocene (Messinian) evaporite deposits of the Silician Basin. *Sedimentology* **1976**, *23*, 729–760. [[CrossRef](#)]
30. Orti, F.; Rosell, L. The Ninyerola Gypsum unit: An example of cyclic, lacustrine sedimentation (Middle Miocene, E Spain). *J. Iber. Geol.* **2007**, *33*, 249–260.
31. Cody, R.D.; Cody, A.M. Gypsum nucleation and crystal morphology in analog saline terrestrial environments. *J. Sediment. Res.* **1988**, *582*, 247–255.
32. Sarg, J.F. The sequence stratigraphy, sedimentology, and economic importance of evaporite-carbonate transitions: A review. *Sediment. Geol.* **2001**, *140*, 9–42. [[CrossRef](#)]
33. Mahboudi, A.; Moussavi-Harami, R.; Carpenter, S.J.; Aghaei, A.; Collins, L.B. Petrographical and geochemical evidences for paragenetic sequence interpretation of diagenesis in mixed siliciclastic–carbonate sediments: Mozduran Formation (Upper Jurassic), south of Agh-Darband, NE Iran. *Carbonates Evaporites* **2010**, *25*, 231–246. [[CrossRef](#)]
34. Kinsman, D.J.J. Gypsum and anhydrite of recent age, Trucial coast, Persian Gulf. In *Second Symposium on Salt*; Northern Ohio Geological Society: Cleveland, OH, USA, 1966.
35. Yağmurlu, F.; Helvacı, C. Sedimentological characteristics and facies of the evaporite-bearing Kirmir Formation (Neogene), Beypazari Basin, central Anatolia, Turkey. *Sedimentology* **1994**, *41*, 847–860. [[CrossRef](#)]
36. Koşun, E.; Çiner, A. Zara güneyi (Sivas Havzası) karasal-sığ denizel Miyosen çökellerinin litostratigrafisi ve fasiyes özellikleri. *Bull. Min. Res. Exp.* **2002**, *125*, 65–88.
37. Warren, J.K. *Evaporites*; Blackwell Science: Hoboken, NJ, USA, 1999; 1035p.
38. Hardie, L.A.; Smoot, J.P.; Eugster, H.P. Saline lakes and their deposits: A sedimentological approach. In *Modern and Ancient Lakes Sediments*; Matter, A., Tucker, M.E., Eds.; Int. Assoc. Sedimentol. Spec. Publ.: London, UK, 1978; Volume 2, pp. 7–41.
39. Handford, C.R. Sedimentology and evaporite genesis in a Holocene continental-sabkha playa basin Bristol Dry Lake, California. *Sedimentology* **1982**, *29*, 239–253. [[CrossRef](#)]
40. Schreiber, B.C.; Decima, A. Sedimentary facies produced under evaporitic environments: A review. *Memorie Societa Geologica Italiana* **1976**, *16*, 111–116.
41. Aref, M.; Attia, O.; Wali, A. Facies and depositional environment of the Holocene evaporites in the Ras Shukeir area, gulf of Suez, Egypt. *Sediment. Geol.* **1997**, *110*, 123–145. [[CrossRef](#)]
42. Calvert, S.E.; Pedersen, T.F. Sedimentary geochemistry of manganese: Implications for the environment of formation of manganeseiferous black shales. *Econ. Geol.* **1996**, *91*, 36–47. [[CrossRef](#)]
43. Vallentyne, J.R. Isolation of pyrite spherules from recent sediments. *Limnol. Oceanogr.* **1963**, *8*, 16–30. [[CrossRef](#)]
44. Chamley, H. *Clay Sedimentology*; Springer: Berlin/Heidelberg, Germany, 1989; pp. 623–668.
45. Sümengen, M. *Başkale-L52 Paftası: Turkey 1/100.000 ölçekli Jeoloji Haritaları Serisi*, 1st ed.; Min. Res. Exp.: Ankara, Turkey, 1980; 63p.
46. Kushnir, J. The composition and origin of brines during the Messinian desiccation event in the Mediterranean basin as deduced from concentrations of ions coprecipitated with gypsum and anhydrite. *Chem. Geol.* **1982**, *35*, 333–350. [[CrossRef](#)]
47. Palmer, M.R.; Helvacı, C.; Fallick, A.E. Sulphur, sulphate oxygen and strontium isotope composition of Cenozoic Turkish evaporites. *Chem. Geol.* **2004**, *209*, 341–356. [[CrossRef](#)]
48. Pye, K.; Krinsley, D.H. Diagenetic carbonate and evaporite minerals in Rotliegend aeolian sandstones of the southern North Sea: Their nature and relationship to secondary porosity. *Clay Miner.* **1986**, *21*, 443–457. [[CrossRef](#)]
49. Haug, G.H.; Gunther, D.; Peterson, L.C.; Sigman, D.M.; Highen, K.A.; Aeschlimann, B. Climate and the collapse of Maya Civilization. *Science* **2003**, *299*, 1731–1735. [[CrossRef](#)]
50. Reinhardt, N.; Proenza, J.A.; Villanova-de-Benavent, C.; Aiglsperger, T.; Bover-Arnal, T.; Torro, L.; Salas, R.; Dziggel, A. Geochemistry and mineralogy of rare earth elements (Ree) in bauxitic ores of the Catalan coastal range, NE Spain. *Minerals* **2018**, *8*, 562. [[CrossRef](#)]
51. Pettijohn, F.J.; Potter, P.E.; Siever, R. *Sand and Sandstone*; Springer: Berlin/Heidelberg, Germany, 1973; p. 631.
52. Li, B.L.; Zhou, C.H. Climatic variation and desertification in West sandy land of northeast China plain. *J. Nat. Resour.* **2001**, *16*, 234–239.
53. Adatte, T.; Keller, G.; Stinnesbeck, W. Late Cretaceous to early Paleocene climate and sea-level fluctuations. the Tunisian record. *Palaeogeogr. Palaeoclimatol. Palaeoecol.* **2002**, *178*, 165–196. [[CrossRef](#)]

54. Khormali, F.; Abtahi, A.; Owliaei, H.R. Late Mesozoic-Cenozoic clay mineral rocks of southern Iran and their palaeoclimatic implications. *Clay Miner.* **2005**, *40*, 191–203. [[CrossRef](#)]
55. Deconinck, E.; Hancock, T.; Coomans, D.; Massart, D.L.; Vander Heyden, Y. Classification of drugs in absorption classes using the classification and regression trees (CART) methodology. *J. Pharm. Biomed. Anal.* **2005**, *39*, 91–103. [[CrossRef](#)]
56. Hernandez-Hinojosa, V.; Montiel-Garcia, P.C.; Armstrong-Altrin, J.S.; Kasper-Zubillaga, J.J. Textural and geochemical characteristics of beach sands along the western Gulf of Mexico. *Carpathian J. Earth Environ. Sci.* **2018**, *13*, 161–174. [[CrossRef](#)]
57. Roy, P.D.; Smykatz-Kloss, W.; Sinha, R. Late Holocene geochemical history inferred from Sambhar and Didwana playa sediments, Thar Desert, India: Comparison and synthesis. *Quat. Int.* **2006**, *144*, 84–98. [[CrossRef](#)]
58. Usdowski, E. Der Einbau von Sr in Gips und Anhydrit. In *Annual Meeting Deutsche Mineral.*; Arnold Gesell-Frances: Berlin, Germany, 1967.
59. Hasselöv, M.; Lyvén, D.; Haraldsson, C.; Sirinawin, W. Determination of continuous size and trace element distribution of field-flow fractionation with ICPMS. *Anal. Chem.* **1999**, *71*, 3497–3502. [[CrossRef](#)]
60. Krauskopf, K.B. *Introduction to Geochemistry*; McGraw-Hill Book Company: New York, NY, USA, 1979.
61. Rushdi, A.I.; McManus, J.; Collier, R.W. Marine barite and celestite saturation in seawater. *Mar. Chem.* **2000**, *69*, 19–31. [[CrossRef](#)]
62. Playa, E.; Cendon, D.I.; Trave, A.; Chivas, A.; Garcia, A.R. Non-marine evaporites with both inherited marine and continental signatures the Gulf of Carpentaria, Australia, at ~70 ka. *Sediment. Geol.* **2007**, *201*, 267–285. [[CrossRef](#)]
63. Bahadori, A.; Carranza, E.J.M.; Soleimani, B. Geochemical analysis of evaporite sedimentation in Gachsaran Formation, Zeloil oil field, southwest Iran. *J. Geochem. Explor.* **2011**, *111*, 97–112. [[CrossRef](#)]
64. Chen, Z.; Ming, Z.; Qiang, J.; Yongjun, R. Distribution of sterane maturity parameters in a lacustrine basin and their control factors. A case study from the Dongying Sag, East China. *Pet. Sci.* **2011**, *8*, 290–301. [[CrossRef](#)]
65. Averty, K.B.; Paytan, A. Empirical partition coefficients for Sr and Ca in marine barite: Implications for reconstructing seawater Sr and Ca concentrations. *Geochem. Geophys. Geosystems* **2003**, *4*, 1–14. [[CrossRef](#)]
66. Krefci-Graf, K. Geochemische Faziesdiagnostik. *Freib. Forsch.* **1966**, *224*, 1–80.
67. Wignall, P.B.; Yers, K.J. Interpreting benthic oxygen levels in mudrocks: A new approach. *Geology* **1988**, *16*, 452–555. [[CrossRef](#)]
68. Kumar, A.; Verma, J.P. Does plant microbe interaction confer stress tolerance in plants: A review? *Microbiol. Res.* **2018**, *207*, 41–52. [[CrossRef](#)]
69. Hallberg, R.O. A geochemical method for investigation of palaeoredox conditions in sediments. *Ambio Spec. Rep.* **1976**, *4*, 139–147.
70. Raiswell, R.; Plant, J. The incorporation of trace elements into pyrite during diagenesis of black shales, Yorkshire, England. *Econ. Geol.* **1980**, *75*, 684–699. [[CrossRef](#)]
71. Patteson, J.H.; Ramsden, A.R.; Dale, L.S.; Fardy, J.J. Geochemistry and mineralogical residences of trace elements in oil shales from Julia Creek, Queensland, Australia. *Chem. Geol.* **1986**, *55*, 1–16. [[CrossRef](#)]
72. Guo, P.; Chiyang, L.; Peng, W.; Ke, W.; Haili, Y.; Li, B. Geochemical behavior of rare elements in Paleogene saline lake sediments of the Qaidam Basin NE Tibetan Plateau. *Carbonates Evaporites* **2019**, *34*, 359–372. [[CrossRef](#)]
73. Gaillardet, J.; Viers, J.; Dupre, B. Trace elements in river waters. In *Treatise on Geochemistry*; Holland, H.D., Turekian, K.K., Eds.; Elsevier: Amsterdam, The Netherlands, 2004; pp. 225–272.
74. McArthur, J.M.; Howarth, R.J.; Bailey, T.R. Strontium isotope stratigraphy: Best fit to the marine Sr-isotope curve for 0–509 Ma and accompanying look-up table for deriving numerical age. *J. Geol.* **2001**, *109*, 155–170. [[CrossRef](#)]
75. Lu, F.H.; Meyers, W.J. Sr, S, and O (SO₄) isotopes and the depositional environments of the Upper Miocene evaporites, Spain. *J. Sediment. Res.* **2003**, *73*, 444–450. [[CrossRef](#)]
76. Banner, J.L.; Musgrove, M.; Capo, R.C. Tracing groundwater evolution in a limestone aquifer using Sr isotopes: Effects of multiple sources of dissolved ions and mineral-solution reactions. *Geology* **1994**, *22*, 681–690. [[CrossRef](#)]
77. Veizer, J.; Compston, W. ⁸⁷Sr/⁸⁶Sr composition of sea water during the Phanerozoic. *Geochim. Et Cosmochim. Acta* **1974**, *38*, 1461–1484. [[CrossRef](#)]
78. Burke, W.H.; Denison, R.E.; Hetherington, E.A.; Koepnick, R.B.; Nelson, H.F.; Otto, J.B. Variation of seawater ⁸⁷Sr/⁸⁶Sr throughout Phanerozoic time. *Geology* **1982**, *10*, 516–519. [[CrossRef](#)]
79. Veizer, J.; Compston, W.; Clauer, N.; Schidlowski, M. ⁸⁷Sr/⁸⁶Sr in Late Proterozoic carbonates: Evidence for a mantle event at 900 Ma ago. *Geochim. Cosmochim. Acta* **1983**, *47*, 295–302. [[CrossRef](#)]
80. Derry, L.A.; Brasier, M.D.; Corfield, R.M.; Rozanov, A.Y.; Zhuravlev, A.Y. Sr and C isotopes in Lower Cambrian carbonates from the Siberian craton: A paleoenvironmental record during the Cambrian explosion. *Earth Planet. Sci. Lett.* **1994**, *128*, 671–681. [[CrossRef](#)]
81. Veizer, J.; Compston, W. ⁸⁷Sr/⁸⁶Sr in Precambrian carbonates as an index of crustal evolution. *Geochim. Et Cosmochim. Acta* **1976**, *40*, 905–914. [[CrossRef](#)]
82. Pearce, J.A.; Bender, J.F.; De Long, S.E.; Kidd, W.S.F.; Low, P.J.; Güner, Y.; Şaroğlu, F.; Yılmaz, Y.; Moorbath, S.; Mitchell, J.G. Genesis of collision volcanism in Eastern Anatolia, Turkey. *J. Volcanol. Geotherm. Res.* **1990**, *44*, 189–229. [[CrossRef](#)]
83. Arslan, M.; Temizel, İ.; Abdioğlu, E.; Kolaylı, H.; Yücel, C.; Boztuğ, D.; Şen, C. ⁴⁰Ar–³⁹Ar dating, whole-rock and Sr–Nd–Pb isotope geochemistry of post-collisional Eocene volcanic rocks in the southern part of the Eastern Pontides (NE Turkey): Implications for magma evolution in extension-induced origin. *Contrib. Mineral. Petrol.* **2013**, *166*, 113–142. [[CrossRef](#)]
84. Holser, W.T. Catastrophic chemical events in the history of the oceans. *Nature* **1977**, *267*, 403–408. [[CrossRef](#)]

85. Claypool, G.E.; Holser, W.T.; Kaplan, I.R.; Sakai, H.; Zak, I. The age curves of sulfur and oxygen isotopes in marine sulfate and their mutual interpretation. *Chem. Geol.* **1980**, *28*, 199–260. [[CrossRef](#)]
86. Strauss, H. The isotopic composition of sedimentary sulfur through time. *Palaeogeogr. Palaeoclimatol. Palaeoecol.* **1997**, *132*, 97–118. [[CrossRef](#)]
87. Schröder, S.; Bekker, A.; Beukes, N.J.; Strauss, H.; Van Niekerk, H.S. Rise in seawater sulphate concentration associated with the Paleoproterozoic positive carbon isotope excursion: Evidence from sulphate evaporites in the ~2.2–2.1 Gyr shallow-marine Lucknow Formation, South Africa. *Terra Nova* **2008**, *20*, 108–117. [[CrossRef](#)]
88. Shields, G.A.; Mills, B.J.W. Sulfur cycle imbalance and environmental change during the Ediacaran Period. *Estud. Geológicos* **2019**, *75*, e114. [[CrossRef](#)]
89. Holser, W.T.; Kaplan, I.R. Isotope geochemistry of sedimentary sulfates. *Chem. Geol.* **1966**, *1*, 93–135. [[CrossRef](#)]
90. Barkov, N.I.; Nikolaev, V.I.; Strizhov, V.P. On the genesis of mirabilite in the McMurdo Sound region, Antarctica. *Lithol. Miner. Resour.* **1995**, *30*, 374–379.
91. Zak, I.; Sakai, H.; Kaplan, I.R. Factors controlling the $^{18}\text{O}/^{16}\text{O}$ and $^{34}\text{S}/^{32}\text{S}$ isotope ratios of ocean sulfates, evaporites and interstitial sulfates from modern deep sea sediments. In *Isotope Marine Chemistry*; Goldberg, E.D., Horibe, Y., Saruhashi, K., Eds.; Rokakuho: Tokyo, Japan, 1980; pp. 339–373.
92. Cavazza, W.; Cattò, S.; Zattin, M.; Okay, A.I.; Reiners, P. Thermochronology of the Miocene Arabia-Eurasia collision zone of southeastern, Turkey. *Geosphere* **2018**, *14*, 5. [[CrossRef](#)]
93. Kent, P.E. The emergent Hormoz salt plugs of southern Iran. *J. Pet. Geol.* **1979**, *2*, 117–144. [[CrossRef](#)]
94. Houghton, M.L. Geochemistry of the Proterozoic Hormuz Evaporites, Southern Iran. Master's Thesis, University of Oregon, Eugene, OR, USA, 1980.
95. Soffel, H.C.; Forster, H. Polar wander path of Central East Iran microplate including new results. *Neues Jahrb. Für Geol. Und Paläontologie* **1984**, *168*, 165–172. [[CrossRef](#)]
96. Banerjee, D.M.; Mazumdar, A. On the Late Neoproterozoic-Early Cambrian transition events in parts of East Gondwanaland. *Gondwana Res.* **1999**, *2*, 199–211. [[CrossRef](#)]
97. Alavi, M. Regional stratigraphy of the Zagros Fold-Thrust Belt of Iran and its proforeland evolution. *Am. J. Sci.* **2004**, *304*, 1–20. [[CrossRef](#)]
98. Talbot, C.; Aftabi, P.; Chemia, Z. Potash in a salt mushroom at Hormoz Island, Hormoz Strait, Iran. *Ore Geol. Rev.* **2008**, *35*, 317–332. [[CrossRef](#)]
99. Motamedi, H.; Sepehr, M.; Sherkati, S.; Pourkermani, M. Multi-Phase Hormuz salt diapirism in the Southern Zagros, SW Iran. *J. Pet. Geol.* **2010**, *34*, 29–43. [[CrossRef](#)]
100. Oberhansli, R.; Candan, O.; Bousquet, R.; Rimmele, G.; Okay, A.; Goff, J. Alpine high pressure evolution of the eastern Bitlis complex, SE Turkey. *Geol. Soc. Lond. Spec. Publ.* **2010**, *340*, 461–483. [[CrossRef](#)]
101. Scheffler, F.; Oberhansli, R.; Pourteau, A.; Immenhauser, A.; Candan, O. Sedimentologic to metamorphic processes recorded in the high-pressure/low-temperature Mesozoic Rosetta Marble of Anatolia. *Int. J. Earth Sci.* **2016**, *105*, 225–246. [[CrossRef](#)]
102. Scheffler, F.; Immenhauser, A.; Pourteau, A.; Natalicchio, M.; Candan, O.; Oberhansli, R. A lost Tethyan evaporitic basin: Evidence from a Cretaceous hemipelagic meta-selenite—Red chert association in the Eastern Mediterranean realm. *Sedimentology* **2019**, *66*, 2627–2660. [[CrossRef](#)]
103. Ocakoğlu, F. Repetitive subtidal to coastal sabkha cycles from a Lower–Middle Miocene marine sequence, eastern Sivas Basin. *Turk. J. Earth Sci.* **2001**, *10*, 17–34.
104. Rahimpour-Bonab, H.; Kalantarzadeh, Z. Origin of secondary potash deposits; a case from Miocene evaporites of NW Central Iran. *J. Asian Earth Sci.* **2005**, *25*, 157–166. [[CrossRef](#)]
105. Rahimpour-Bonab, H.; Shariatnia, Z.; Siemann, M.G. Origin and geochemistry of Miocene marine evaporites associated with red beds: Great Kavir Basin, Central Iran. *Geol. J.* **2007**, *42*, 37–54. [[CrossRef](#)]
106. Hüsing, S.K.; Zachariasse, W.J.; Van Hinsbergen, D.J.; Krijgsman, W.; Inceöz, M.; Harzhauser, M.; Mandic, O.; Kroh, A. Oligocene Miocene basin evolution in SE Anatolia, Turkey: Constraints on the closure of the eastern Tethys gateway. *Geol. Soc. Lond. Spec. Publ.* **2009**, *311*, 107–132. [[CrossRef](#)]
107. Ayyıldız, T.; Varol, B.; Karakaş, Z.; Sözeri, K. Miocene evaporites in the intermountain Tuzluca–Iğdır Neogene Basin, Eastern Turkey. EGU General Assembly: Vienna, Austria, 2012.
108. Kavooosi, M.A.; Sherkati, S. Depositional environments of the Kalhur Member evaporites and tectonosedimentary evolution of the Zagros fold–thrust belt during Early Miocene in south westernmost of Iran. *Carbonates Evaporites* **2012**, *27*, 55–69. [[CrossRef](#)]
109. Yeşilova, Ç.; Helvacı, C. Lice Formasyonu Evaporitleri ve Killerinin Ekonomik Önemi: Baykan–Kurtalan–Şirvan Bölgesi (Siirt). *J. Inst. Nat. Appl. Sci.* **2012**, *17*, 72–83.
110. Yeşilova, Ç.; Helvacı, C. Stratigraphy and sedimentology north of Batman and Siirt, Turkey. *Turk. Assoc. Pet. Geol. Bull.* **2013**, *23*, 7–49.
111. Güngör Yeşilova, P.; Helvacı, C. Diagenesis and paleogeographic development of Oligocene evaporites of the Germik Formation (Kurtalan, SW Siirt), Turkey. *Bull. Earth. Sci.* **2013**, *34*, 1–22.
112. Abdioğlu, E.; Arslan, M.; Aydınçakır, D.; Gündoğan, İ.; Helvacı, C. Stratigraphy, mineralogy and depositional environment of the evaporite unit in the Aşkale (Erzurum) sub-basin, Eastern Anatolia (Turkey). *J. Afr. Earth Sci.* **2015**, *111*, 100–112. [[CrossRef](#)]

113. Ribes, C.; Kergaravat, C.; Bonnel, C.; Crumeyrolle, P.; Callot, J.P.; Poisson, A.; Temiz, H.; Ringenbach, J.C. Fluvial sedimentation in a salt-controlled mini-basin: Stratal patterns and facies assemblages, Sivas Basin, Turkey. *Sedimentology* **2015**, *62*, 1513–1545. [[CrossRef](#)]
114. Soleimani, B.; Bahadori, A. The Miocene Gachsaran Formation evaporite cap rock, Zeloi oilfield, SW Iran. *Carbonates Evaporites* **2015**, *30*, 287–306. [[CrossRef](#)]
115. Kangal, Ö.; Özgen -Erdem, N.; Varol, B. Depositional states of Eğribucak inner basin (terrestrial to marine evaporite and carbonate) from the Sivas Basin (Central Anatolia, Turkey). *Turk. J. Earth Sci.* **2016**, *25*, 127–146.
116. Kergaravat, C.; Ribes, C.; Callot, J.-P.; Legeay, E.; Ringenbach, J.-C. Minibasins and salt canopies in foreland fold-and-thrust belts: The central Sivas Basin, Turkey. *Tectonics* **2016**, *35*, 1342–1366. [[CrossRef](#)]
117. Varol, B.; Şen, Ş.; Ayyıldız, T.; Sözeri, K.; Karakaş, Z.; Metais, G. Sedimentology and stratigraphy of Cenozoic deposits in the Kağızman–Tuzluca Basin, northeastern Turkey. *Int. J. Earth Sci.* **2016**, *105*, 107–137. [[CrossRef](#)]
118. Güngör-Yeşilova, P.; Helvacı, C. Petrographic study and geochemical investigation of the evaporites associated with Germik formation (Siirt Basin, Turkey). *Carbonates Evaporites* **2017**, *32*, 177–194. [[CrossRef](#)]
119. Ribes, C.; Lopez, M.; Kergaravat, C.; Crumeyrolle, P.; Poisson, A.; Callot, J.-P.; Paquette, J.-L.; Ringenbach, J.-C. Facies partitioning and stratal pattern in salt-controlled marine to continental mini-basins: Examples from the late Oligocene to early Miocene of the Sivas Basin, Turkey. *Mar. Pet. Geol.* **2018**, *93*, 468–496. [[CrossRef](#)]
120. Yeşilova, Ç.; Helvacı, C.; Carrillo, E. Evaporitic sedimentation in the Southeastern Anatolian Foreland Basin, Newinsights on the Neotethys closure. *Sediment. Geol.* **2018**, *369*, 13–27. [[CrossRef](#)]
121. Güngör Yeşilova, P.; Gökmen, D. The paleodepositional environment, diagenetic and depositional conditions of the Middle-Late Miocene Koluz gypsum member (NE Van, Eastern Turkey). *Carbonates Evaporites* **2020**, *35*, 76. [[CrossRef](#)]
122. Güngör Yeşilova, P.; Yeşilova, Ç. Depositional basin, diagenetic conditions and source of Miocene evaporites in the Tuzluca Basin in Northeastern Anatolia, Turkey: Geochemical evidence. *Geochem. Int.* **2021**, *59*, 1293–1310. [[CrossRef](#)]
123. Güngör Yeşilova, P.; Yavuz, Ş. Sedimentological and mineralogical-petrographic characteristics of Miocene evaporitic deposits (SW Erzincan). *MANAS* **2021**, *9*, 169–183. [[CrossRef](#)]
124. Müller, D.W.; Mueller, P.A. Origin and age of the Mediterranean Messinian evaporites implications from Sr isotopes. *Earth Planet. Sci. Lett.* **1991**, *107*, 1–12. [[CrossRef](#)]
125. Pierre, C. Sedimentation and diagenesis in restricted marine basins. In *The Marine Environment*; Fritz, P., Fontes, J.C.H., Eds.; Elsevier: Amsterdam, The Netherlands, 1989; pp. 257–315.
126. Veizer, J.; Godderis, Y.; François, L.M. Evidence for decoupling of atmospheric CO₂ and global climate during the Phanerozoic eon. *Nature* **2000**, *408*, 698–701. [[CrossRef](#)] [[PubMed](#)]
127. Taylor, B.E.; Wheeler, M.C.; Nordstrom, D.K. Oxygen and sulfur compositions of sulfate in acid mine drainage: Evidence for oxidation mechanisms. *Nature* **1984**, *308*, 538–541. [[CrossRef](#)]
128. Nriagu, J.O.; Rees, C.E.; Mekhtiyeva, V.L.Y.; Lein, A.; Fritz, P.; Drimmie, R.J.; Pankina, R.G.; Robinson, B.W.; Krouse, H.R. Hydrosphere. In *Stable Isotopes: Natural and Anthropogenic Sulfur in the Environment*; Krouse, H.R., Grinenko, V.A., Eds.; John Wiley and Sons: Oxford, UK, 1991; pp. 177–266.
129. Lu, F.H.; Meyers, W.J. Sr, S, O, SO₄ isotopes and quantitative models of Messinian gypsum, the Nijar Basin, Spain (Abstract). In Proceedings of the International Applied Isotope Geochemistry (AIG-2) Conference, Calgary, AB, Canada, 1997; Available online: <https://www.iagc-society.org/AGI> (accessed on 2 February 2023).
130. Taberner, C.; Marshall, J.D.; Hendry, J.P.; Pierre, C.; Thirlwall, M.F. Celestite formation, bacterial sulphate reduction and carbonate cementation of Eocene reefs and basinal sediments (Iguualada, NE Spain). *Sedimentology* **2002**, *49*, 171–190. [[CrossRef](#)]

Disclaimer/Publisher’s Note: The statements, opinions and data contained in all publications are solely those of the individual author(s) and contributor(s) and not of MDPI and/or the editor(s). MDPI and/or the editor(s) disclaim responsibility for any injury to people or property resulting from any ideas, methods, instructions or products referred to in the content.